PREDICTION OF THE SUBSURFACE STRESS STATE IN A

MOVING SEMI-INFINITE SOLID FOR LOADING CON-

DITIONS REPRESENTING TOOL-WORKPIECE

CONTACT IN ULTRA-PRECISION

MACHINING

By

ANDREW CHARLES LOEBER

Bachelor of Science
Purdue University
West Lafayette, Indiana
1988

Bachelor of Science
Montana State University
Bozeman, Montana
1992

Submitted to the Faculty of the
Graduate College of the
Oklahoma State University
in partial fulfillment of
the requirements of
the Degree of
MASTER OF SCIENCE
December, 1996

PREDICTION OF THE SUBSURFACE STRESS STATE IN A

MOVING SEMI-INFINITE SOLID FOR LOADING CON-

DITIONS REPRESENTING TOOL-WORKPIECE

CONTACT IN ULTRA-PRECISION

MACHINING

Thesis Approved:

Don a. Lucca

Thesis Adviser

C E Price

Gary Z. Young

Larise Volynets

Thomas C. Collins

Dean of the Graduate College

ACKNOWLEDGMENTS

I wish to express my thanks to my major adviser, Dr. Don Lucca, for his guidance during the preparation of this work. I would also like to thank my other committee members, Drs. Christopher Price, Gary Young and Larisa Volynets.

I also thank my parents for their support and encouragement.

TABLE OF CONTENTS

LIST OF TABLES

LIST OF FIGURES

NOMENCLATURE

C_d	dilatation wave speed
C_s	shear wave speed
E	Young's modulus
e	dilatation
$\dot{e}^e_{ij}$, $\dot{e}^P_{ij}$, $\dot{e}_{ij}$	elastic, plastic and total incremental strains
F_c, F_t	cutting and thrust forces
$f(\xi)$, $f'(s)$	Fourier integral transform and its inverse
G	shear modulus
k	yield strength in shear
l	slider half-contact length
l_f	contact length of flank face
P, Q	vertical and horizontal force per unit depth
p_0, q_0	maximum normal and tangential surface stresses
r_1, r_2	distances from loading point in concentrated force model
s_{ij}	deviatoric stress components
t_0	uncut chip thickness
V	speed of semi-infinite body
$\dot{w}^P$	incremental plastic work per unit volume
x, y, z	Cartesian coordinates
Y	uniaxial yield strength
$(\varepsilon_{ii})_r$	residual normal strain
ϕ	stress function
$(\gamma_{\xi\eta})_r$	residual shear strain

λ, μ	Lamé's constants
μ_f	coefficient of friction
ν	Poisson's ratio
θ_1, θ_2	included angles in concentrated force model
ρ	mass density
σ_1, σ_3	maximum and minimum principal stresses
σ_{ij}	stress on face i in direction j
$(\sigma_{ij})_r$	residual stress
$(\sigma_{ij})'_r$	pseudo-residual stress
τ_{max}	maximum shear stress
ξ, η, ζ	dimensionless coordinates for x, y, z

Chapter 1

Introduction

There has been significant interest of late in developing a better understanding of the process mechanics which govern the removal of material by cutting with sub-micrometer depths of cut. Recently both experimental [11] and theoretical [10] studies of the resulting force system in the ultra-precision machining of ductile materials have been reported. It has been observed in the experimental study of ultra-precision machining at sub-micrometer uncut chip thicknesses that the dominant length scale may become the contact length at the tool-workpiece interface [11]. It has been further observed that the cutting force is much greater than the thrust force at these uncut chip thicknesses, so that sliding and plowing, rather than chip formation, may be the dominant energy dissipative processes. As a consequence, shearing in the shear zone and rake face friction may possibly be neglected in the idealized model of the ultra-precision machining process. For such a case, a sliding indentation model of the tool-workpiece interaction may be appropriate. Figure 1-1 is a schematic of the tool-workpiece interface under the conditions described above. Here, t_0 is the uncut chip thickness, and l_f is the contact length at the tool-workpiece interface.

Since the tool is much stiffer than the workpiece, and the length scale of the workpiece is much larger than its interface with the tool, the sliding indentation model may be idealized as a rigid slider (tool) on an elastic/elastoplastic, semi-infinite body (workpiece). Figure 1-2 shows this model as a stationary slider of length $2l$, where l is the half-contact length, with a semi-infinite body moving in the negative x-direction.

This model will be used to determine the elastic stresses in a moving semi-infinite body
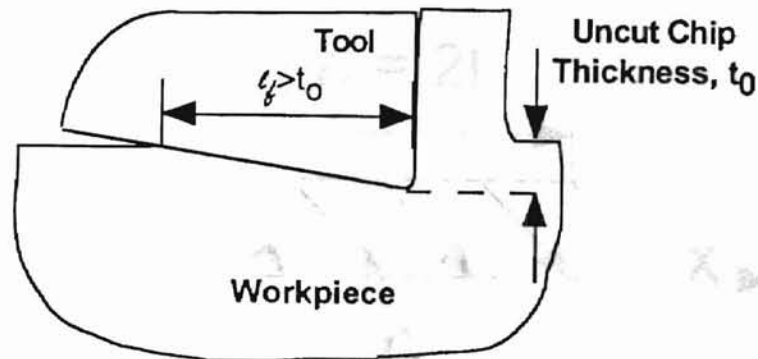
Figure 1-1: Tool-Workpiece Interface in Ultra-Precision Machining.

under a slider exerting a constant surface pressure. The solution of the elastic stresses will be used as the initial conditions for a numerical model used to determine the elastoplastic stress field and residual stress for several experimentally measured loading conditions previously reported [11]. These elastic stresses, as well as the elastoplastic and the resulting residual stresses, will be calculated by a modified version of a previous, non-working version (the version available for use in this study) of the FORTRAN program employed, but not included in [13]. To calculate the elastic fields correctly, it was necessary to change the program so that all constants are calculated within subroutines, rather than in the main program.

The present study was conducted to reconcile the residual stresses reported in [13] using the Merwin-Johnson method with the FEM results reported in [16]. The expressions used for the elastic stress gradients in the non-working program yielded the same residual stresses as [13]. After modification of those expressions, which will be discussed later, the residual stress solution agreed with the reported FEM solution[16].

Previously reported solutions [14] for the elastic stress fields for a stationary elastic semi-infinite body with an elliptical surface load will be used to verify the stress fields for a stationary elastic semi-infinite body with a constant load. At a low sliding speed, the dilatation and shear wave speeds are small relative to the sliding speed, so dynamic effects

2
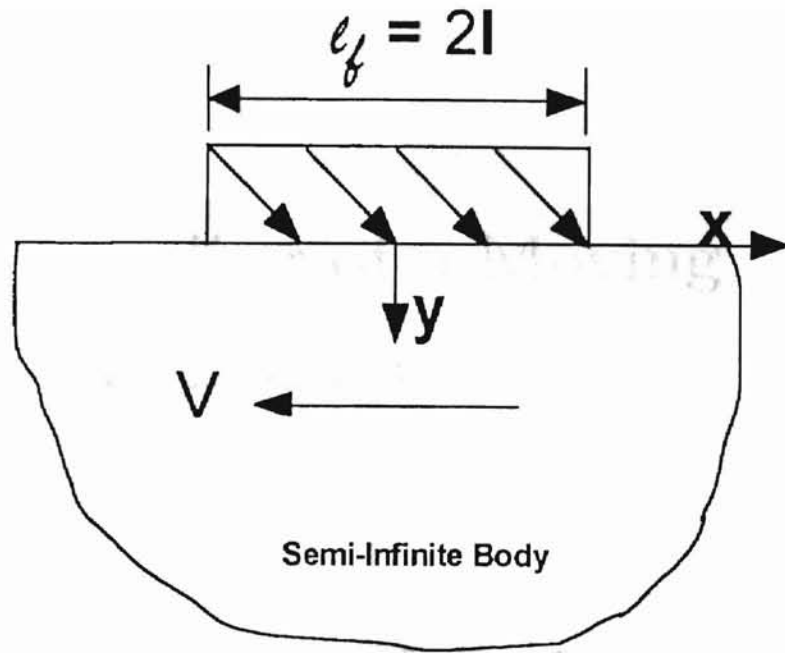
Figure 1-2: Idealization of the Tool-Workpiece Interface as a Sliding Indentation Contact.

are negligible. For this case, the elastodynamic stress fields with a constant pressure can be compared to those of a stationary semi-infinite body with a constant pressure.

According to Saint Venant's principle, given different surface pressure distributions, the overall elastic stress fields should be the same at points far away from the load as long the total applied force and the geometry of the body remain the same. Therefore, the numerical solution for the elastostatic stress fields with constant pressure may in turn be verified by comparing it to the elastostatic fields under an elliptical surface pressure, for which there is a closed-form solution [14].

Chapter 2

Elastic Loading of a Moving Semi-Infinite Solid

2.1 Elastic Stress Field

This chapter presents the solutions for the elastostatic stress fields in a semi-infinite body moving underneath a rigid slider exerting an elliptical and a constant surface pressure, and the elastodynamic stress fields underneath a rigid slider exerting a constant surface pressure.

2.1.1 Elastostatic Stress Field

Concentrated Surface Load

Figure 2-1 shows a semi-infinite elastic solid loaded by a concentrated line indenter which is infinitely long in the direction perpendicular to the x- and y-directions. The force per unit length has vertical and tangential components P and Q, respectively. An Airy's stress function, ϕ, may be expressed as [13]:

$$\phi = -\frac{1}{\pi}[P\,r_1\theta_1\sin\theta_1 - Q\,r_2\theta_2\sin\theta_2] \qquad (2.1)$$

where r_i and θ_i , i = 1,2 are distances from the loading point and included angles from the direction of loading to the point of interest, respectively. Using the geometric relations of

4
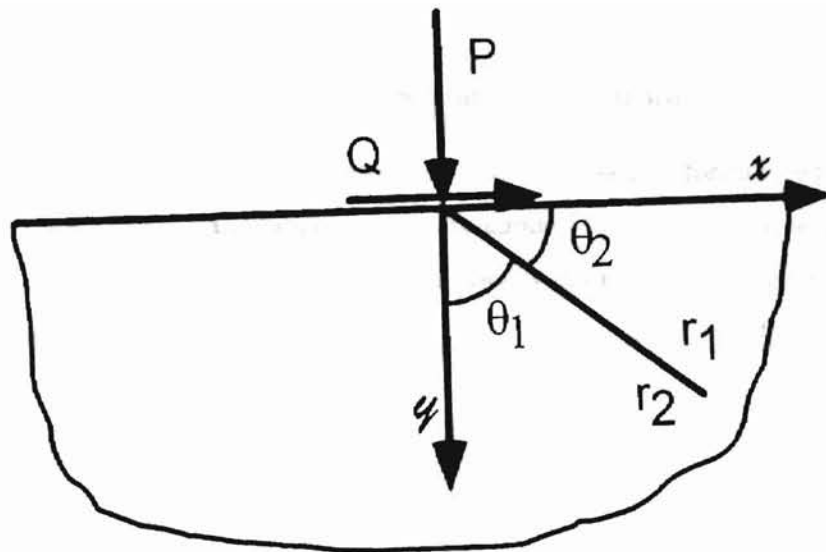
Figure 2-1: Geometry of an Inclined Concentrated Load.

Figure 2-1,

$$x = r_1 \sin \theta_1, \ y = r_2 \sin \theta_2 \tag{2.2a}$$

$$\theta_1 = \arctan \frac{x}{y}, \ \theta_2 = \arctan \frac{y}{x} \tag{2.2b}$$

ϕ can be expressed in terms of x and y. The stress fields can now be determined as:

$$\sigma_{xx} = \frac{\partial^2 \phi}{\partial y^2} \ , \ \sigma_{yy} = \frac{\partial^2 \phi}{\partial x^2} \ , \ \sigma_{xy} = -\frac{\partial^2 \phi}{\partial x \partial y} \tag{2.3}$$

Hence,

$$\sigma_{xx} = \frac{2P}{\pi} (\mu_f x - y) \frac{x^2}{(x^2 + y^2)^2} \tag{2.4a}$$

$$\sigma_{yy} = \frac{2P}{\pi} (\mu_f x - y) \frac{y^2}{(x^2 + y^2)^2} \tag{2.4b}$$

5

$$\sigma_{xy} = \frac{2P}{\pi}(\mu_f x - y)\frac{xy}{(x^2 + y^2)^2} \tag{2.4c}$$

where $\mu_f = Q/P$.

Distributed Surface Load-Elliptical Surface Distribution

The elastostatic stresses due to a distributed surface load can be formulated using the stress fields for a concentrated load. Equations 2.4 are applied to a differential length $d\xi$ at $x = \xi$, integrating over the contact length. For an elliptically distributed surface load over a length $2l$, the stresses acting at the boundary of the semi-infinite body are[14], [16]:

$$\sigma_{yy} = \begin{cases} 0 & for \; |x| > l \\ -p_0\left(1 - \frac{x^2}{l^2}\right)^{\frac{1}{2}} & for \; |x| \le l \end{cases} \tag{2.5a}$$

$$\sigma_{xy} = \begin{cases} 0 & for \; |x| > l \\ q_0\left(1 - \frac{x^2}{l^2}\right)^{\frac{1}{2}} & for \; |x| \le l \end{cases} \tag{2.5b}$$

where p_0 and q_0 are the maximum normal and tangential stresses acting at $(x, y) = (0, 0)$ and $2l$ is the contact length.

Rewriting Equations 2.4 for a concentrated load acting at $x = \xi$ and integrating with respect to ξ from $-l$ to l gives the stress fields due to the elliptically distributed load:

$$\sigma_{xx} = \frac{2q_0}{\pi l}\int_{-l}^{l}\frac{(l^2 - \xi^2)^{\frac{1}{2}}}{y}\frac{(x-\xi)^3 y}{[y^2 + (x-\xi)^2]^2}d\xi + \frac{2p_0}{\pi l}\int_{-l}^{l}\frac{(l^2-\xi^2)^{\frac{1}{2}}}{y}\frac{y^2(x-\xi)^2}{[y^2+(x-\xi)^2]^2}d\xi \tag{2.6a}$$

$$\sigma_{yy} = \frac{2q_0}{\pi l}\int_{-l}^{l}\frac{(l^2 - \xi^2)^{\frac{1}{2}}}{y}\frac{(x-\xi)y^3}{[y^2 + (x-\xi)^2]^2}d\xi + \frac{2p_0}{\pi l}\int_{-l}^{l}\frac{(l^2-\xi^2)^{\frac{1}{2}}}{y}\frac{y^4}{[y^2+(x-\xi)^2]^2}d\xi \tag{2.6b}$$

$$\sigma_{xy} = \frac{2q_0}{\pi l}\int_{-l}^{l}\frac{(l^2 - \xi^2)^{\frac{1}{2}}}{y}\frac{(x-\xi)^2 y^2}{[y^2 + (x-\xi)^2]^2}d\xi + \frac{2p_0}{\pi l}\int_{-l}^{l}\frac{(l^2-\xi^2)^{\frac{1}{2}}}{y}\frac{y^3(x-\xi)}{[y^2+(x-\xi)^2]^2}d\xi \tag{2.6c}$$

6

Integrating Equations 2.6, the stresses in the semi-infinite solid due to the elliptically distributed load are [14]:

$$\sigma_{xx} = -\frac{q_0}{\pi}[(2x^2 - 2l^2 - 3y^2)\psi + 2\pi\frac{x}{l} + 2(l^2 - x^2 - y^2)\frac{x}{l}\Psi] - \frac{p_0}{\pi}y[\frac{l^2 + 2x^2 + 2y^2}{l}\Psi - \frac{2\pi}{l} - 3x\psi]$$

(2.7a)

$$-\frac{p_0}{\pi}y[\frac{l^2 + 2x^2 + 2y^2}{l}\Psi - \frac{2\pi}{l} - 3x\psi]$$

$$\sigma_{yy} = -\frac{q_0}{\pi}y^2\psi - \frac{p_0}{\pi}\frac{y}{\pi}[l\Psi - x\psi]$$

(2.7b)

$$\sigma_{xy} = -\frac{q_0}{\pi}[(l^2 + 2x^2 + 2y^2)\frac{y}{l}\Psi - 2\pi\frac{y}{l} - 3xy\psi] - \frac{p_0}{\pi}y^2\psi$$

(2.7c)

where

$$\psi = \frac{\pi}{k_1}\frac{1 - \left(\frac{k_2}{k_1}\right)^{\frac{1}{2}}}{\left[\frac{k_2}{k_1}\left[2\left(\frac{k_2}{k_1}\right)^{\frac{1}{2}} + \left(\frac{k_1 + k_2 - 4l^2}{k_1}\right)\right]^{\frac{1}{2}}\right]^{\frac{1}{2}}}$$

(2.7d)

$$\Psi = \frac{\pi}{k_1}\frac{1 + \left(\frac{k_2}{k_1}\right)^{\frac{1}{2}}}{\left[\frac{k_2}{k_1}\left[2\left(\frac{k_2}{k_1}\right)^{\frac{1}{2}} + \left(\frac{k_1 + k_2 - 4l^2}{k_1}\right)\right]^{\frac{1}{2}}\right]^{\frac{1}{2}}}$$

(2.7e)

$$k_1 = (l^2 + x^2) + y^2$$

(2.7f)

$$k_2 = (l^2 - x^2) + y^2$$

(2.7g)

The maximum normal and tangential stresses at the boundary, p_0 and q_0, are related to the resultant force per unit length P and Q of Equations 2.4 as:

$$p_0 = \frac{2P}{\pi l}$$

(2.8a)

7

$$q_0 = \frac{2Q}{\pi l} \qquad (2.8b)$$

The σ_{xx} component of the stress at the boundary $y = 0$ can be derived by setting $y = 0$ in Equation 2.6a and evaluating the integral [14]. This stress is given by

$$\sigma_{xx} = \begin{cases} 2q_0 \left[\frac{x}{l} - \left(\frac{x^2}{l^2} - 1 \right)^{\frac{1}{2}} \right] & for \ x > l \\[3mm] 2q_0 \left[\frac{x}{l} + \left(\frac{x^2}{l^2} - 1 \right)^{\frac{1}{2}} \right] & for \ x < -l \\[3mm] 2q_0 \frac{x}{l} - p_0 \left(1 - \frac{x^2}{l^2} \right)^{\frac{1}{2}} & for \ |x| \leq l \end{cases} \qquad (2.9)$$

For any finite normal elongation, the normal strain ϵ_{zz} is zero for an infinite width. Therefore, plane strain conditions apply, and:

$$\sigma_{zz} = \nu(\sigma_{xx} + \sigma_{yy}) \qquad (2.10)$$

Distributed Surface Load-Constant Surface Distribution

Although an elliptical stress distribution is often assumed to exist, even between elasto-plastic solids, the actual distribution tends to be more uniform across the interface in elastoplastic solids when yielding occurs at the contact area [5], [7]. Therefore, a constant surface pressure distribution is probably more appropriate to the tool-workpiece interface in ultra-precision machining, if yielding actually occurs at this interface.

Expressions similar to Equations 2.6 can be formulated using the same approach as for an elliptical distribution. The surface conditions for a constant distribution are:

$$\sigma_{yy} = \begin{cases} 0 & for \ |x| > l \\ -p_0 & for \ |x| \leq l \end{cases} \qquad (2.11a)$$

$$\sigma_{xy} = \begin{cases} 0 & for \ |x| > l \\ q_0 & for \ |x| \leq l \end{cases} \qquad (2.11b)$$

8

The equations for the stress fields are:

$$\sigma_{xx} = \frac{2q_0}{\pi} \int_{-l}^{l} \frac{(x-\xi)^3}{[(x-\xi)^2 + y^2]^2} d\xi + \frac{2p_0}{\pi} \int_{-l}^{l} \frac{(x-\xi)^2 y}{[(x-\xi)^2 + y^2]^2} d\xi \qquad (2.12a)$$

$$\sigma_{yy} = \frac{2q_0}{\pi} \int_{-l}^{l} \frac{(x-\xi)y^2}{[(x-\xi)^2 + y^2]^2} d\xi + \frac{2p_0}{\pi} \int_{-l}^{l} \frac{y^3}{[(x-\xi)^2 + y^2]^2} d\xi \qquad (2.12b)$$

$$\sigma_{xy} = \frac{2q_0}{\pi} \int_{-l}^{l} \frac{(x-\xi)^2 y}{[(x-\xi)^2 + y^2]^2} d\xi + \frac{2p_0}{\pi} \int_{-l}^{l} \frac{(x-\xi)y^2}{[(x-\xi)^2 + y^2]^2} d\xi \qquad (2.12c)$$

and $\sigma_{zz} = \nu(\sigma_{xx} + \sigma_{yy})$ for plane strain.

The above equations were solved by Seo [13] using a ten-point Gaussian quadrature technique; however, results for σ_{xx}, σ_{yy} and σ_{xy} were not reported. The same method was used in the modified code of the present work to determine these stresses. These results are discussed in the next chapter.

2.1.2 Elastodynamic Stress Fields: Distributed Surface Load-Constant Surface Distribution

For the case of a semi-infinite body moving with velocity V in the negative x-direction beneath a stationary, constant surface load (Figure 1-2), a Fourier integral transform method was used to determine the elastodynamic stress fields in [13] and in the present study. This method is often used to simplify the equations arising in these problems [1], [9] and have been used in the analysis of anisotropic bodies [2], [8] and sliders of varying shapes [3], [4]. The body's speed is assumed to be much less than the Rayleigh wave speed in the body. That is, elastic surface wave effects are neglected. The body is assumed continuous and homogeneous.

The Fourier integral transform and its inverse transform are defined as:

$$f'(s) = \int_{-\infty}^{\infty} f(\xi)e^{-is\xi} d\xi \qquad (2.13a)$$

$$f(\xi) = \frac{1}{2\pi} \int_{-\infty}^{\infty} f'(s)e^{is\xi} ds \qquad (2.13b)$$

9

where $i = \sqrt{-1}$.

Navier's equations of motion, neglecting body forces, are:

$$\frac{\partial \sigma_{ij}}{\partial x_j} = \rho_0 \frac{\partial^2 u_i}{\partial t^2} \tag{2.14a}$$

$$(\lambda + \mu)\frac{\partial e}{\partial x_i} + \mu \frac{\partial^2 u_i}{\partial x_j \partial x_j} = \rho_0 \frac{\partial^2 u_i}{\partial t^2} \tag{2.14b}$$

where λ and μ are Lamé's constants and e is the dilatation. The boundary conditions are that the surface normal and shear stresses are the same as the applied surface normal and shear pressures, that is, those of Equations 2.11. The integral transform is applied to Equations 2.14 and the boundary conditions. Ordinary differential equations then result, which are solved in the transformed space. The inverse transform is then taken and the complex part rejected. The stress fields are then, in non-dimensional form ($\xi = \frac{x}{l}$, $\eta = \frac{y}{l}$):

$$\sigma_{\xi\xi} = \frac{2}{\pi G_1}\left(-4k \int_0^\infty \frac{\sin s}{s} \cos s\xi \, e^{-js\eta}ds + 2(2 - M^2)\mu_f \int_0^\infty \frac{\sin s}{s} \sin s\xi \, e^{-js\eta}ds \right. \tag{2.15a}$$
$$\left. +(M^2 + 2k^2)\left[(j + \frac{1}{j})\int_0^\infty \frac{\sin s}{s} \cos s\xi \, e^{-ks\eta}ds - 2\mu_f \int_0^\infty \frac{\sin s}{s} \sin s\xi \, e^{-ks\eta}ds\right]\right)$$

$$\sigma_{\eta\eta} = \frac{2}{\pi G_1}\left(4k \int_0^\infty \frac{\sin s}{s} \cos s\xi \, e^{-js\eta}ds - 2(2 - M^2)\mu_f \int_0^\infty \frac{\sin s}{s} \sin s\xi \, e^{-js\eta}ds \right. \tag{2.15b}$$
$$\left. -(2 - M^2)\left[(j + \frac{1}{j})\int_0^\infty \frac{\sin s}{s} \cos s\xi \, e^{-ks\eta}ds - 2\mu_f \int_0^\infty \frac{\sin s}{s} \sin s\xi \, e^{-ks\eta}ds\right]\right)$$

$$\sigma_{\xi\eta} = \frac{2}{\pi G_1}[(j + \frac{1}{j})\left\{(2 - M^2)\mu_f \int_0^\infty \frac{\sin s}{s} \cos s\xi \, e^{-js\eta}ds + 2k \int_0^\infty \frac{\sin s}{s} \sin s\xi \, e^{-js\eta}ds\right\} \tag{2.15c}$$
$$+2k\left\{-2\mu_f \int_0^\infty \frac{\sin s}{s} \cos s\xi \, e^{-ks\eta}ds - (j + \frac{1}{j})\int_0^\infty \frac{\sin s}{s} \sin s\xi \, e^{-ks\eta}ds\right\}]$$

10

where

$$G_1 = (j + \frac{1}{j})(2 - M^2) - 4k, \tag{2.15d}$$

$$j^2 = 1 - M^2, \ k^2 = 1 - \frac{M^2}{N^2}, \tag{2.15e}$$

$M = \frac{V}{C_s}$, $N = \frac{C_d}{C_s}$ and $\mu_f = \frac{Q}{P}$ and C_d and C_s are the dilatation and shear wave speeds in the body. These integrals are evaluated using a ten-point Gauss-Laguerre method, because the integration limits are 0 and ∞.

Stress Gradients

As they will be used to determine the elastoplastic stress field and the residual stresses, the stress gradients (with respect to the sliding direction) of the elastodynamic stress fields were also verified. The central difference technique, in which the quotient of two differences is used to approximate the value of a derivative, was used to check the stress gradients. Using this technique, the stress gradients can be calculated from the stress fields alone, providing a independent check. This technique was used for a few points using the elastic stress field results and compared to the gradients as obtained from Equations 2.16. They did not agree.

In the unmodified program the expressions for the stress gradients are:

$$\frac{\partial \sigma_{\xi\xi}}{\partial \xi} = \frac{2}{\pi G_1}(4k\frac{\partial}{\partial \xi}\int_0^\infty \frac{\sin s}{s}\cos s\xi \ e^{-js\eta}ds - 2(2 - M^2)\mu_f\frac{\partial}{\partial \xi}\int_0^\infty \frac{\sin s}{s}\sin s\xi \ e^{-js\eta}ds$$

$$\tag{2.16a}$$

$$-(M^2 + 2k^2)\left[(j + \frac{1}{j})\frac{\partial}{\partial \xi}\int_0^\infty \frac{\sin s}{s}\cos s\xi \ e^{-ks\eta}ds - 2\mu_f\frac{\partial}{\partial \xi}\int_0^\infty \frac{\sin s}{s}\sin s\xi \ e^{-ks\eta}ds\right])$$

$$\frac{\partial \sigma_{\eta\eta}}{\partial \xi} = \frac{2}{\pi G_1}(-4k\frac{\partial}{\partial \xi}\int_0^\infty \frac{\sin s}{s}\cos s\xi \ e^{-js\eta}ds + 2(2 - M^2)\mu_f\frac{\partial}{\partial \xi}\int_0^\infty \frac{\sin s}{s}\sin s\xi \ e^{-js\eta}ds$$

$$\tag{2.16b}$$

$$+(2 - M^2)\left[(j + \frac{1}{j})\frac{\partial}{\partial \xi}\int_0^\infty \frac{\sin s}{s}\cos s\xi \ e^{-ks\eta}ds - 2\mu_f\frac{\partial}{\partial \xi}\int_0^\infty \frac{\sin s}{s}\sin s\xi \ e^{-ks\eta}ds\right])$$

11

$$\frac{\partial \sigma_{\xi\eta}}{\partial \xi} = -\frac{2}{\pi G_1}[(j+\frac{1}{j})\left\{(2-M^2)\mu_f\frac{\partial}{\partial \xi}\int_0^\infty \frac{\sin s}{s}\cos s\xi\, e^{-js\eta}ds + 2k\frac{\partial}{\partial \xi}\int_0^\infty \frac{\sin s}{s}\sin s\xi\, e^{-js\eta}ds\right\}$$

$$+2k\left\{2\mu_f\frac{\partial}{\partial \xi}\int_0^\infty \frac{\sin s}{s}\cos s\xi\, e^{-ks\eta}ds + (j+\frac{1}{j})\frac{\partial}{\partial \xi}\int_0^\infty \frac{\sin s}{s}\sin s\xi\, e^{-ks\eta}ds\right\}] \tag{2.16c}$$

They should be:

$$\frac{\partial \sigma_{\xi\xi}}{\partial \xi} = \frac{2}{\pi G_1}(-4k\frac{\partial}{\partial \xi}\int_0^\infty \frac{\sin s}{s}\cos s\xi\, e^{-js\eta}ds + 2(2-M^2)\mu_f\frac{\partial}{\partial \xi}\int_0^\infty \frac{\sin s}{s}\sin s\xi\, e^{-js\eta}ds$$

$$+(M^2+2k^2)\left[(j+\frac{1}{j})\frac{\partial}{\partial \xi}\int_0^\infty \frac{\sin s}{s}\cos s\xi\, e^{-ks\eta}ds - 2\mu_f\frac{\partial}{\partial \xi}\int_0^\infty \frac{\sin s}{s}\sin s\xi\, e^{-ks\eta}ds\right]) \tag{2.17a}$$

$$\frac{\partial \sigma_{\eta\eta}}{\partial \xi} = \frac{2}{\pi G_1}(4k\frac{\partial}{\partial \xi}\int_0^\infty \frac{\sin s}{s}\cos s\xi\, e^{-js\eta}ds - 2(2-M^2)\mu_f\frac{\partial}{\partial \xi}\int_0^\infty \frac{\sin s}{s}\sin s\xi\, e^{-js\eta}ds$$

$$-(2-M^2)\left[(j+\frac{1}{j})\frac{\partial}{\partial \xi}\int_0^\infty \frac{\sin s}{s}\cos s\xi\, e^{-ks\eta}ds - 2\mu_f\frac{\partial}{\partial \xi}\int_0^\infty \frac{\sin s}{s}\sin s\xi\, e^{-ks\eta}ds\right]) \tag{2.17b}$$

$$\frac{\partial \sigma_{\xi\eta}}{\partial \xi} = \frac{2}{\pi G_1}[(j+\frac{1}{j})\left\{(2-M^2)\mu_f\frac{\partial}{\partial \xi}\int_0^\infty \frac{\sin s}{s}\cos s\xi\, e^{-js\eta}ds + 2k\frac{\partial}{\partial \xi}\int_0^\infty \frac{\sin s}{s}\sin s\xi\, e^{-js\eta}ds\right\}$$

$$+2k\left\{-2\mu_f\frac{\partial}{\partial \xi}\int_0^\infty \frac{\sin s}{s}\cos s\xi\, e^{-ks\eta}ds - (j+\frac{1}{j})\frac{\partial}{\partial \xi}\int_0^\infty \frac{\sin s}{s}\sin s\xi\, e^{-ks\eta}ds\right\}] \tag{2.17c}$$

The expressions in Equations 2.17 are the negatives of their respective expressions in Equations 2.16.

In this chapter the equations used for the elastostatic stress fields in a semi-infinite body beneath a rigid slider for elliptically and uniformly distributed loads have been developed. The equations for the elastodynamic stress fields beneath a slider with a constant load have also been developed, and the necessary corrections in the program for the stress gradients for this case were noted. In the next chapter the stress field results for the two elastostatic

cases will be used to verify the stress fields for the elastodynamic case. In a later chapter, the elastoplastic stress fields and residual stress results for loading conditions resultant from the ultra-precision machining experiments of [13] will be presented using the corrected stress gradients.

Chapter 3

Elastic Stress Field Results

3.1 Introduction

This chapter presents the elastic stress field results in the form of maximum and minimum principal stresses and the maximum shear stress for the three cases developed in the previous chapter: an isotropic, elastic semi-infinite solid loaded by a stationary rigid slider exerting an elliptical and a constant pressure distribution, and a stationary rigid slider exerting a constant pressure distribution on a moving semi-infinite body. According to Saint Venant's principle, given the same total loading, the stresses should be the same far from the point of loading, though they would differ near the applied load. Also, given the same loading, the effect of a moving semi-infinite solid should be small if the dilatation wave speed and shear wave speed are small. An abbreviated sequence to the verification procedure for the elastic stress fields is presented in Figure 3-1.

All results are for the case $q_0 = \frac{1}{3}p_0$, where p_0 and q_0 are the maximum normal and tangential stresses at the surface underneath the slider. The surface stresses are normalized with respect to p_0. Dimensions are normalized with respect to the half-contact length l of the slider ($\xi = x/l$, $\eta = y/l$). They are plotted for the range of $\xi = [-3, 3]$ and $\eta = [0, 4]$ using a step size of 0.05 in both directions.

For all three cases the surface stresses σ_{yy} and σ_{xy} are known. However, for the two constant loading cases there are singularities in the surface stresses at either end of the slider. Therefore equations similar to Equations 2.9 for the surface stress σ_{xx} can not be

Elastostatic, Elliptical Loading
Closed Form vs. Numerical

Elastostatic
Elliptical Loading vs.
(Closed Form)

Elastostatic
Constant Loading
(Numerical)

Constant Loading
Elastostatic vs. Elastodynamic
(Numerical) (Numerical)
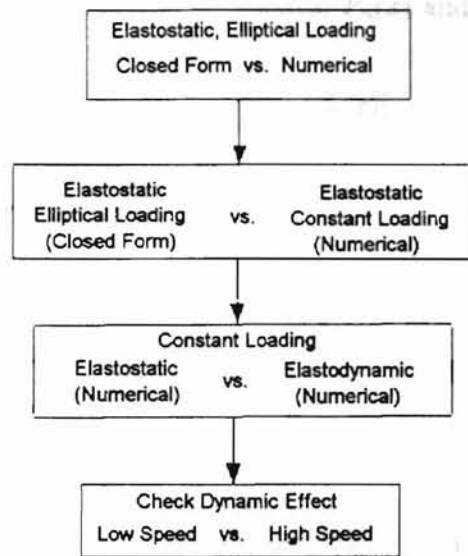
Check Dynamic Effect
Low Speed vs. High Speed

Figure 3-1: Sequence Used to Verify the Elastic Stress Fields.

used. Since σ_{xx} (and therefore σ_{zz} because of plane strain) is undefined at $\mid \xi \mid = 1$, $\eta = 0$, errors are introduced into the numerical stress field solutions at the surface. For this reason the plots for the constant loading cases were prepared without the surface ($\eta = 0$) data. The maximum and minimum principal stresses are given by

$$\sigma_1, \sigma_3 = \frac{\sigma_x + \sigma_y}{2} \pm \sqrt{\left(\frac{\sigma_x - \sigma_y}{2}\right)^2 + \tau_{xy}^2} \qquad (3.1)$$

and the maximum shear stress is

$$\tau_{max} = \frac{(\sigma_1 - \sigma_3)}{2} \qquad (3.2)$$

The stress fields for the elastostatic, constant load case are calculated using ten-point Gaussian quadrature, because it is suited to integrals with finite limits. Gauss's formula is

$$\int_{-1}^{1} f(x)dx = \sum_{i=1}^{n} w_i f(x_i) \qquad (3.3a)$$

15

where x_i is the ith zero of the Legendre polynomial $P_n(x)$ and

$$w_i = \frac{2}{(1-x_i^2)}[P_n(x)] \tag{3.3b}$$

For an arbitrary interval [a,b],

$$\int_a^b f(y)dy = \frac{b-a}{2}\sum_{i=1}^n w_i f(y_i) \tag{3.3c}$$

and

$$y_i = \left(\frac{b-a}{2}\right)x_i + \left(\frac{b+a}{2}\right) \tag{3.3d}$$

The stress fields for the elastodynamic, constant load case are calculated using ten-point Gauss-Laguerre quadrature, because it is suited to integration limits of $[0,\infty]$. The Gauss-Laguerre formula is

$$\int_0^\infty e^{-x}f(x)dx = \sum_{i=1}^n w_i f(x_i) \tag{3.4a}$$

where x_i is the ith zero of the Laguerre polynomial $L_n(x)$ and

$$w_i = \frac{(n!)^2 x_i}{(n+1)^2[L_{n+1}(x_i)]^2} \tag{3.4b}$$

3.2   Evaluation of Numerical Solutions Near the Surface

Since near the surface the numerical solutions are inaccurate because $\sigma_{\xi\xi}$ (and therefore $\sigma_{\zeta\zeta}$ because of plane strain) is undefined at $|\xi| = 1$, $\eta = 0$ for the constant loading cases, Equations 2-6 were evaluated using ten-point Gaussian quadrature to compare with the results of Equations 2-7 through 2-10, the closed-form solution for elliptical loading, so as to see at what depth the numerical solutions become valid. The error in the numerical solutions for the elliptical distribution is in general small. Underneath the slider, errors are within 4% at a dimensionless depth of $\eta = 0.35$ for both principal stresses and the maximum shear stress. Near the edges of the slider there are small zones where there are also errors. For the maximum principal stress the error does not become less than 1% near the trailing edge until $\xi = 1.3$ at a depth of $\eta = 0.05$, for the minimum principal stress and

16

the maximum shear stress on the trailing edge until $\xi = -1.35$ at $\eta = 0.25$ and $\xi = -1.05$ at $\eta = 0.1$, respectively. These stress fields are compared in Figures 3-2, 3-3 and 3-4.

3.3   Maximum Principal Stress

Figures 3-5, 3-6 and 3-7 show the contours of the maximum principal stress,which lies in the $\xi - \eta$ plane, for the elliptical and constant distribution stationary cases and the constant distribution dynamic case. Under the slider these stresses are compressive (negative values), with semi-circular contours shifted somewhat toward the leading-edge, but the contour of any given stress extends somewhat deeper into the body for the constant distribution cases than for the elliptical case. All three show tensile stresses behind the slider. The magnitude of the stresses is greatest at the surface near the slider and becomes smaller away from the slider and deep within the body, as is consistent with the boundary conditions. Figure 3-8 shows a comparison of the three solutions for two contours.

3.4   Minimum Principal Stress

Figures 3-9, 3-10 and 3-11 show the contours of the minimum principal stress for the three cases, which also lie in the $\xi - \eta$ plane. As is the case with the maximum principal stress, the stresses are compressive under the slider with semi-circular stress contours shifted toward the leading edge. As with the maximum principal stress contours, the contours extend somewhat deeper into the body for the constant distribution cases than for the elliptical case. Figure 3-12 shows a comparison of the three solutions for two contours.

3.5   Maximum Shear Stress

Figures 3-13, 3-14 and 3-15 show the maximum shear stress contours for the three cases. As with the principal stresses, under the slider these contours are generally semi-circular and slanted toward the leading edge and extend somewhat deeper into the body for the constant distribution cases. However, a few of the contours fold onto themselves somewhat under the slider and at the trailing edge. This appears not to be an artifact of the numerical

17

modeling, since it is observed in the plot for the closed form, elliptical distribution case as well as the two constant distribution cases. Figure 3-16 shows a comparison of the three solutions for two contours.

3.6   Conclusions

The stress contours for the elliptical and constant distribution stationary cases are similar and become more alike away from the slider and deeper into the body, as they should for the same total load. So it is concluded that the constant distribution solution is correct.

For the dilatation and shear wave speeds involved in the constant distribution dynamic case, there should be very little dynamic effect. The contours for the constant distribution stationary and dynamic cases are nearly identical. To demonstrate that there truly is a dynamic effect, a contour of the von Mises equivalent stress has been plotted in Figure 3-17. For the contour plotted the dynamic effect is only present at very high speeds. It is therefore concluded that the dynamic solution is also correct.
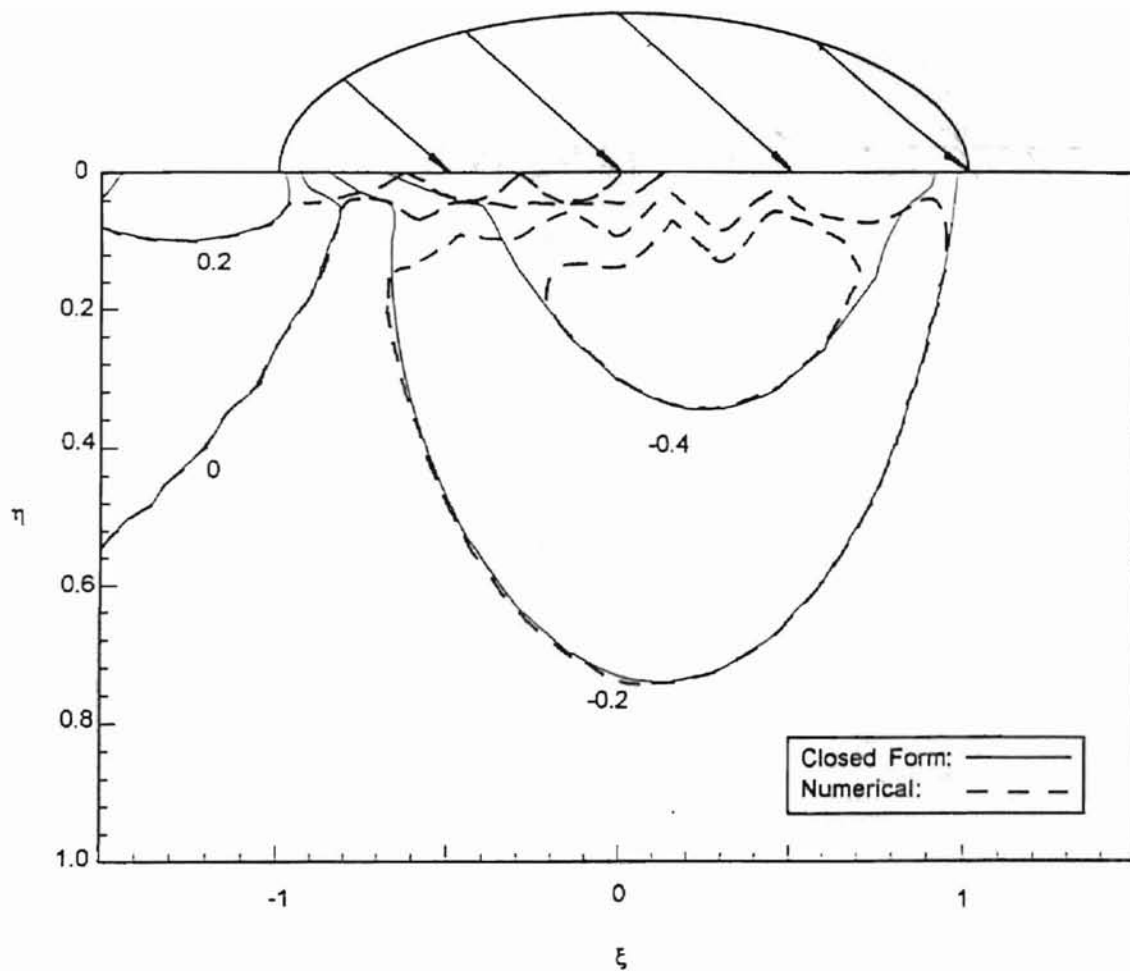
Figure 3-2: Comparison of Closed Form and Numerical Solutions for the Maximum Principal Stress for the Elastostatic Case with Elliptical Loading, $q_0 = 1/3p_0$.
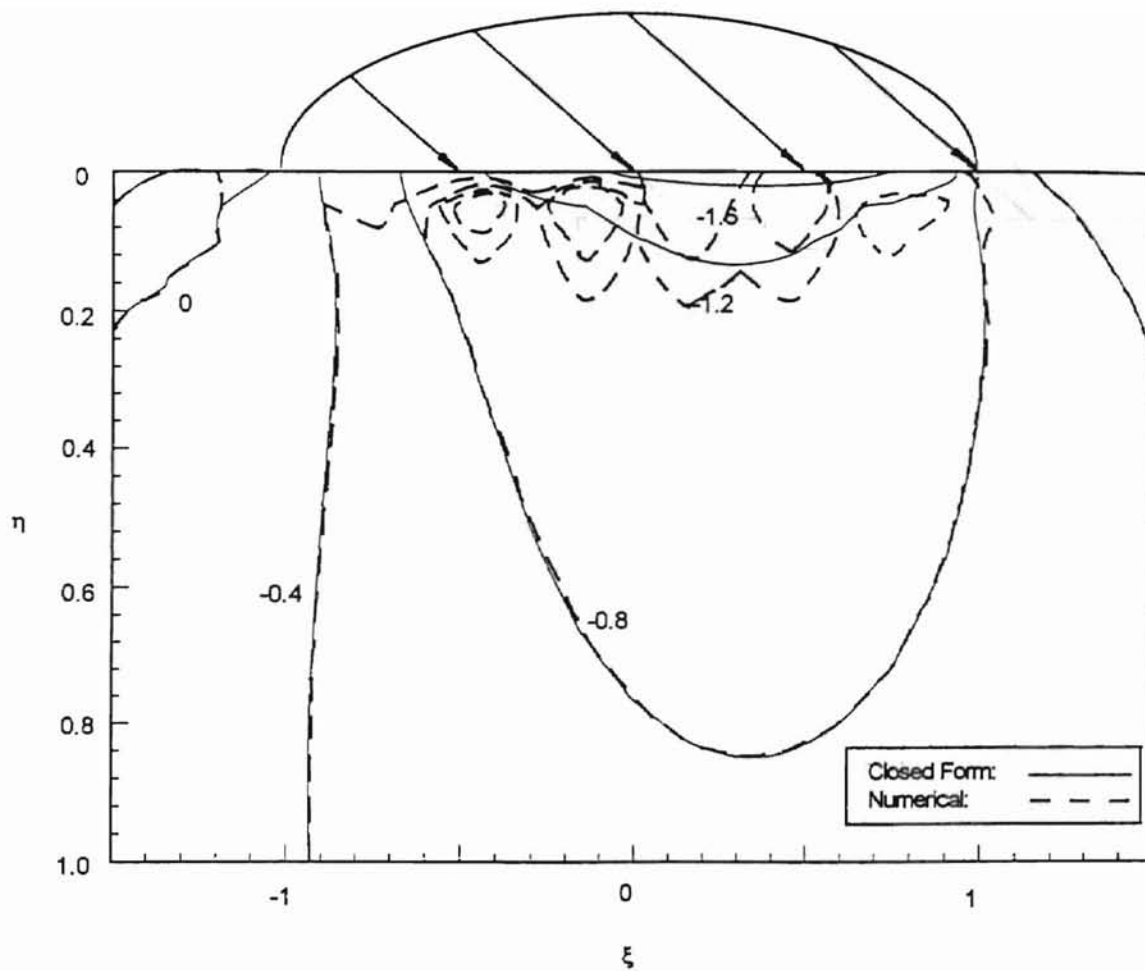
Figure 3-3: Comparison of Closed Form and Numerical Solutions for the Minimum Principal Stress for the Elastostatic Case with Elliptical Loading, $q_0 = 1/3p_0$.
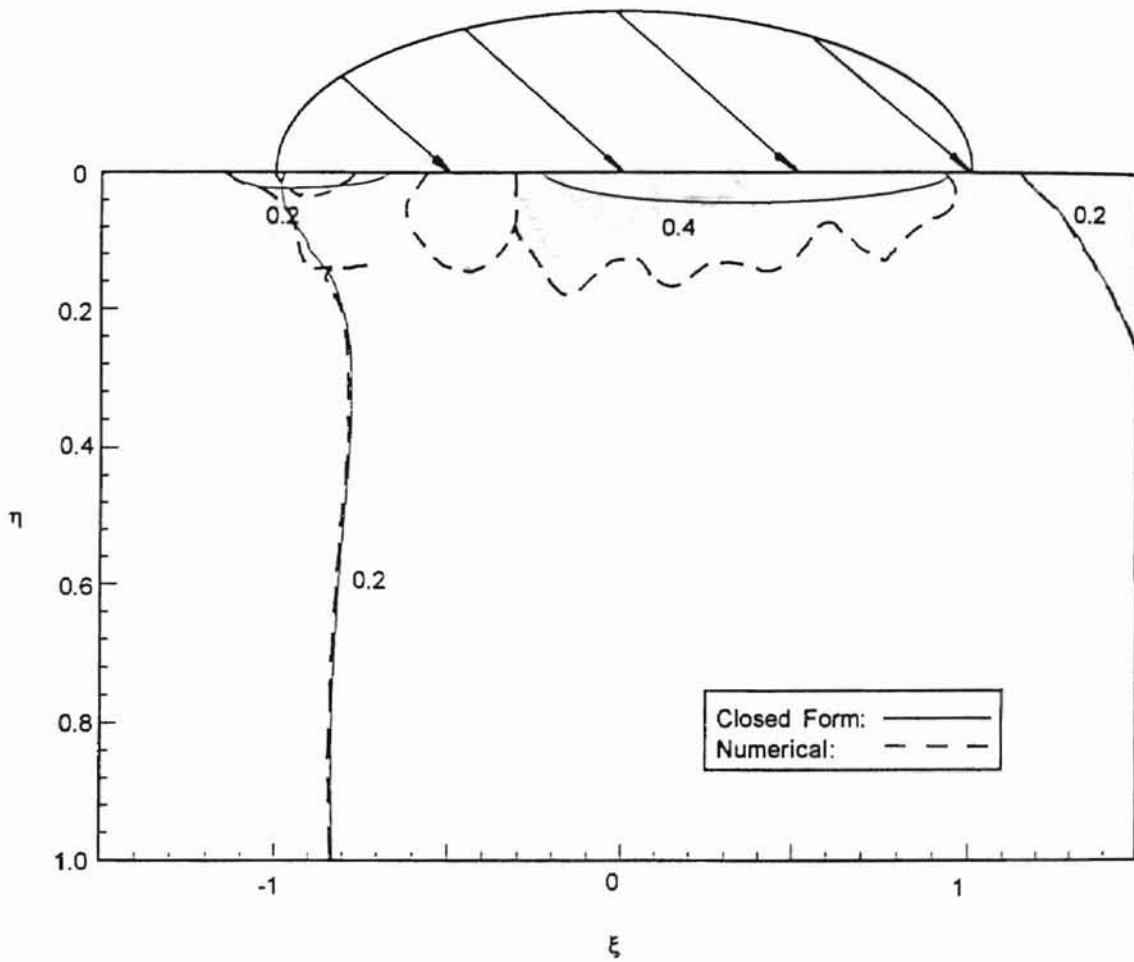
Figure 3-4: Comparison of Closed Form and Numerical Solutions for the Maximum Shear Stress for the Elastostatic Case with Elliptical Loading, $q_0 = 1/3p_0$.
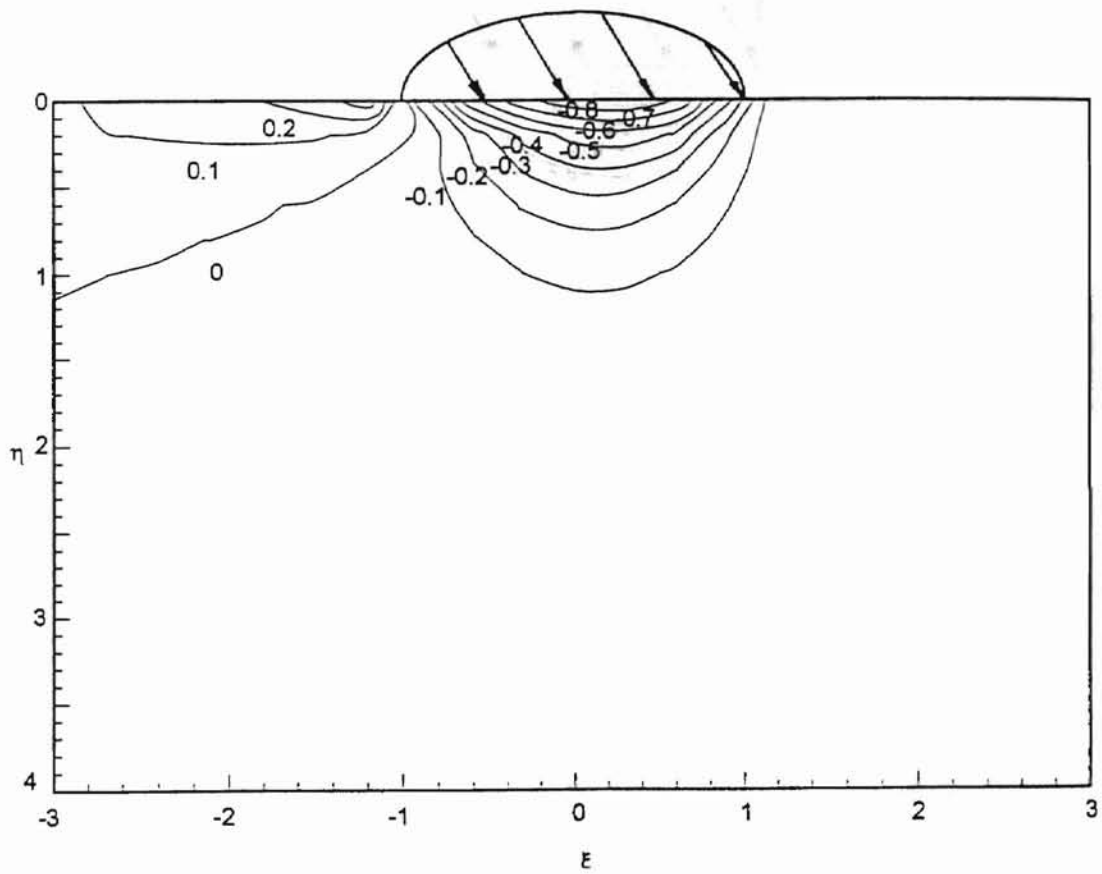
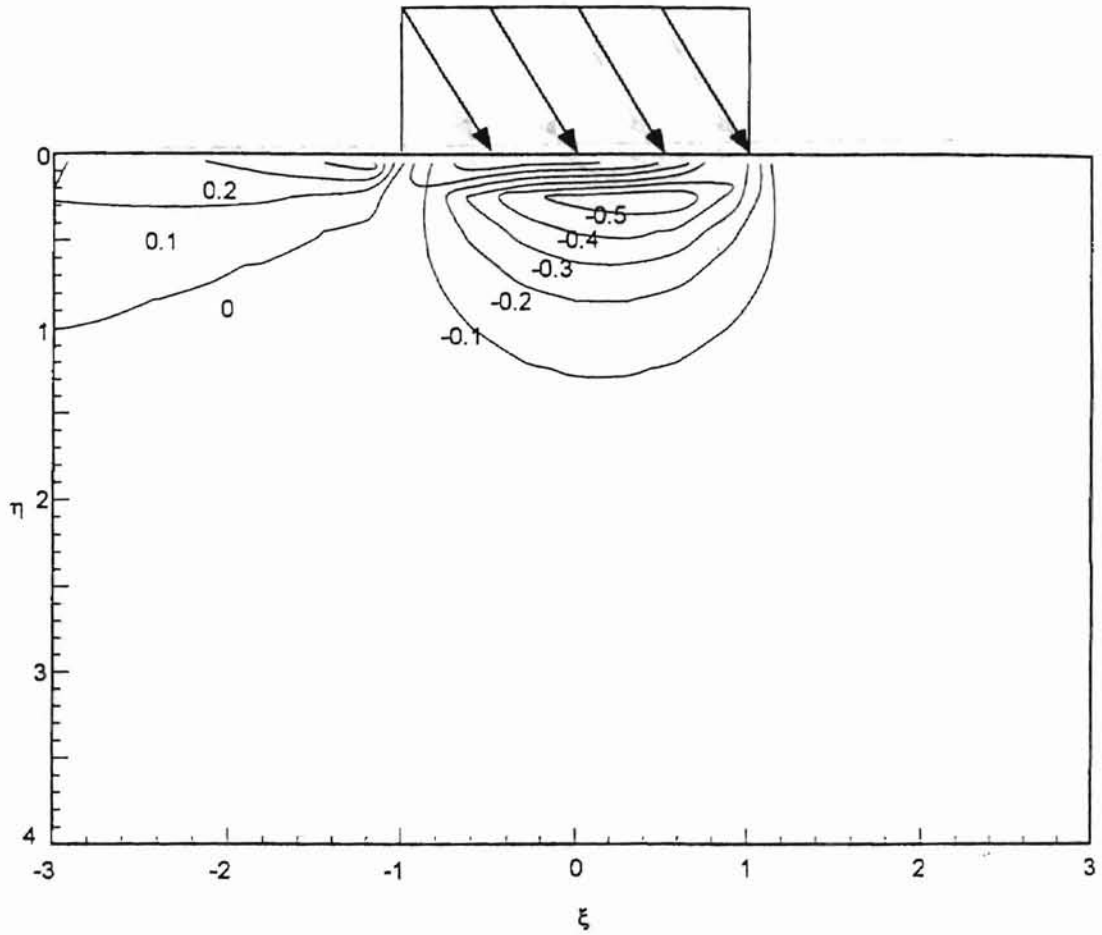Figure 3-5: Maximum Principal Stress for the Elastostatic Case with Elliptical Loading, $q_0 = 1/3p_0$.

Figure 3-6: Maximum Principal Stress for the Elastostatic Case with Constant Loading, $q_0 = 1/3p_0$.
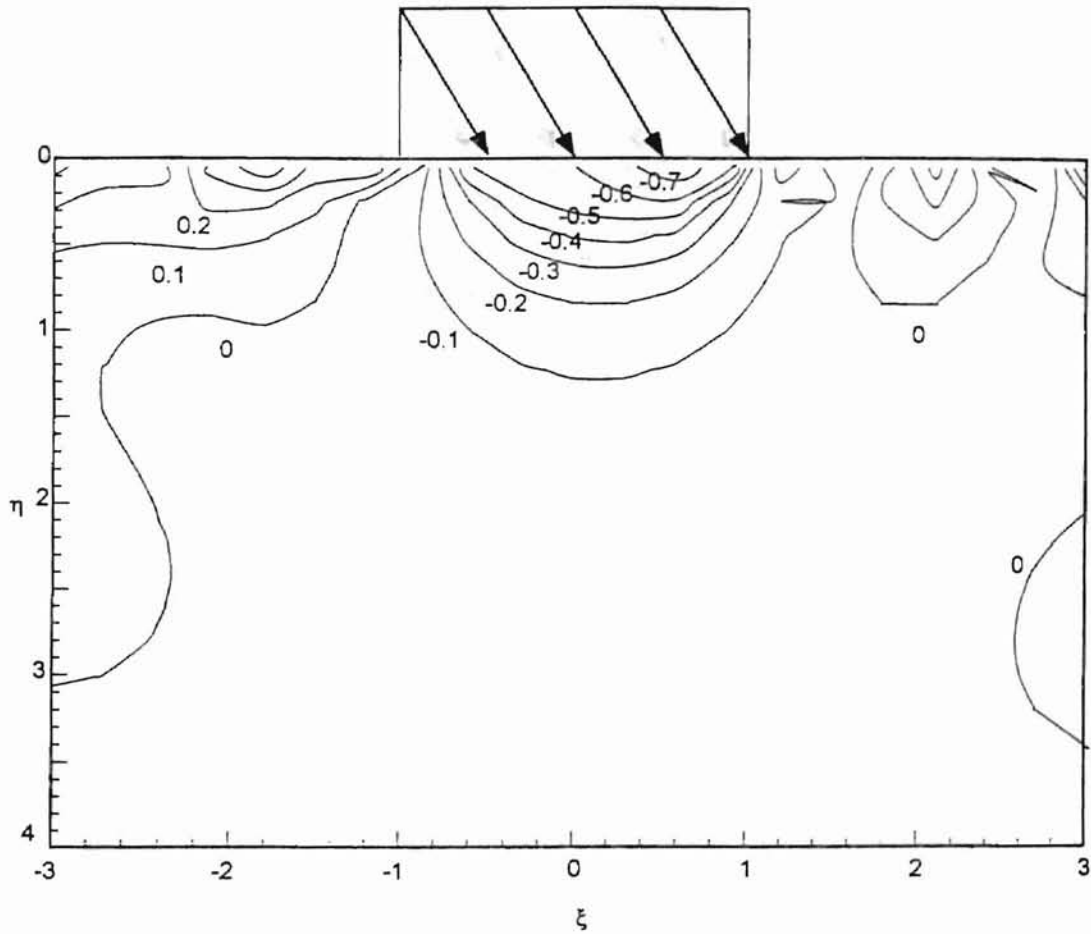
Figure 3-7: Maximum Principal Stress for the Elastodynamic Case with Constant Loading, $q_0 = 1/3 p_0$.

Figure 3-8: Comparison of the Maximum Principal Stress for the Elastostatic, Elliptical and Constant Load Cases, and the Elastodynamic, Constant Load Case, $q_0 = 1/3p_0$.

Figure 3-9: Minimum Principal Stress for the Elastostatic Case with Elliptical Loading, $q_0 = 1/3 p_0$.

Figure 3-10: Minimum Principal Stress for the Elastostatic Case with Constant Loading, $q_0 = 1/3p_0$.

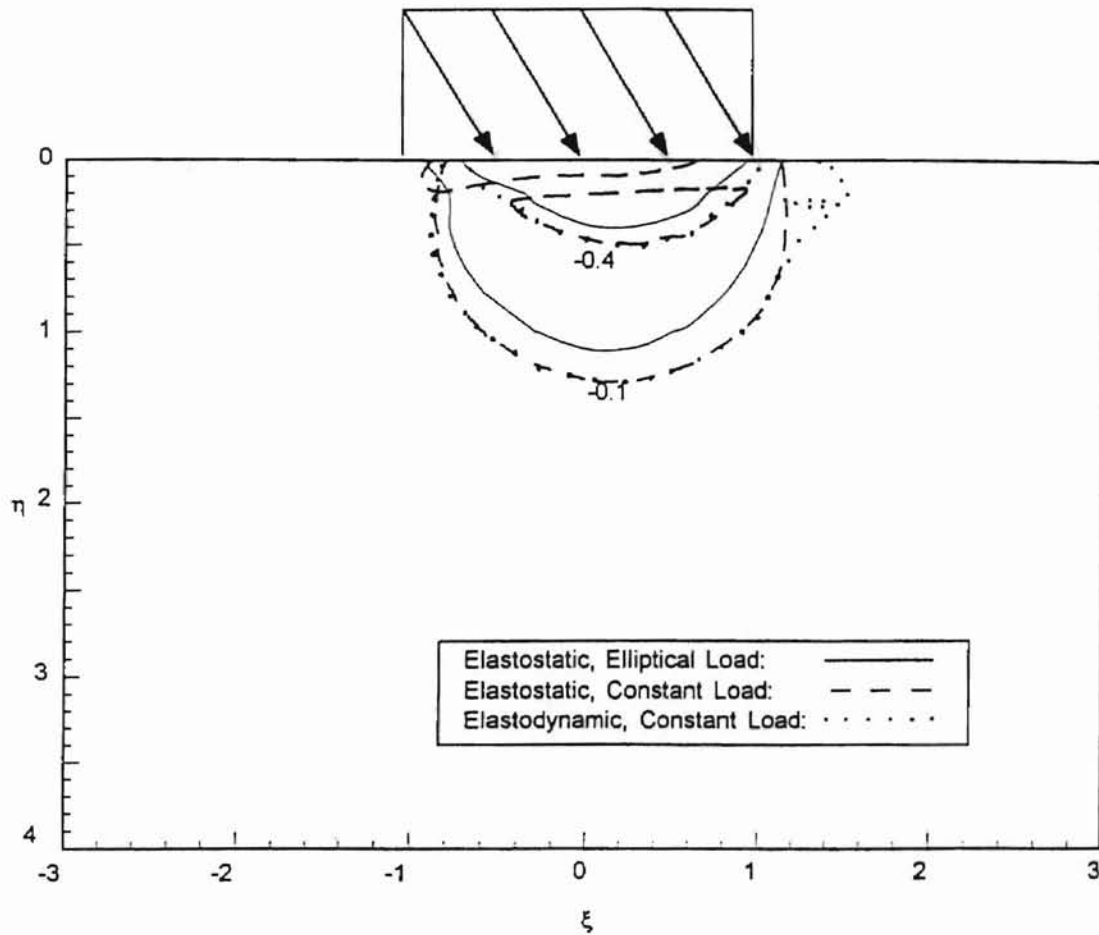Figure 3-11: Minimum Principal Stress for the Elastodynamic Case with Constant Loading, $q_0 = 1/3p_0$.

Figure 3-12: Comparison of the Minimum Principal Stress for the Elastostatic, Elliptical and Constant Load Cases, and the Elastodynamic, Constant Load Case, $q_0 = 1/3p_0$.
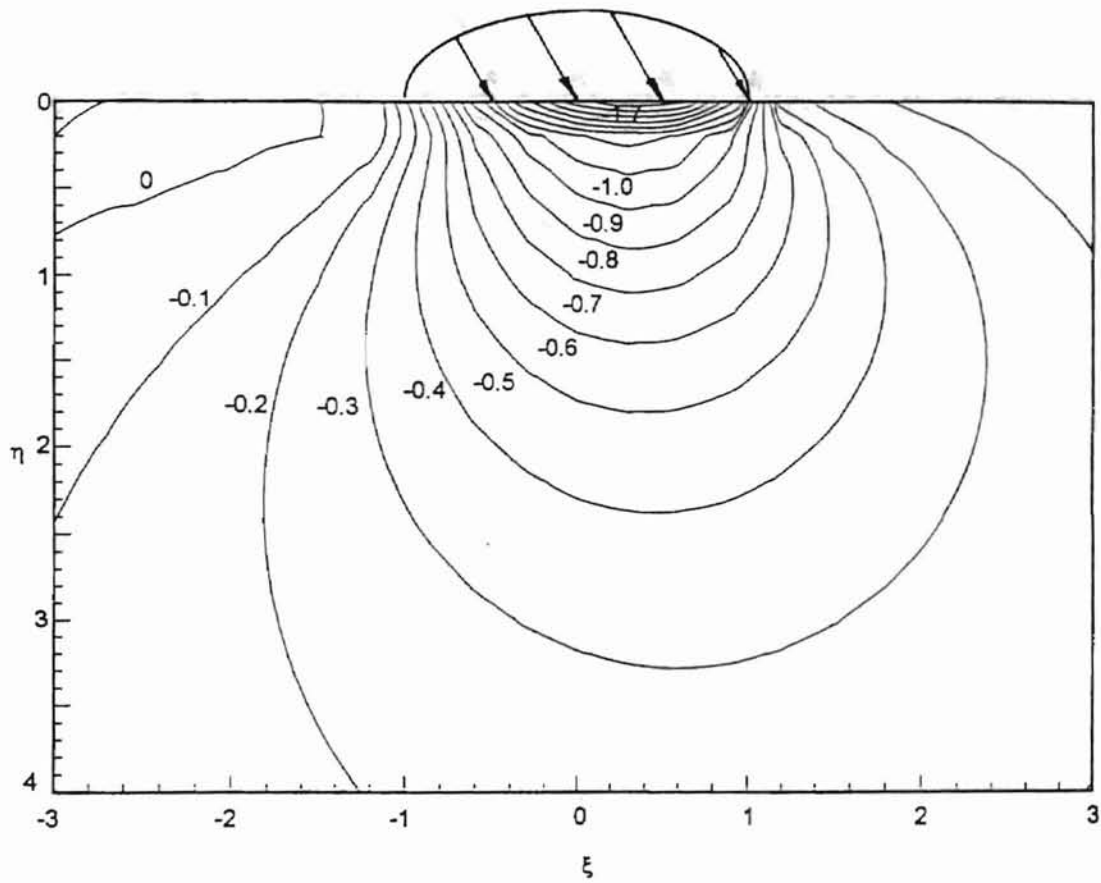
Figure 3-13: Maximum Shear Stress for the Elastostatic Case with Elliptical Loading, $q_0 = 1/3p_0$.
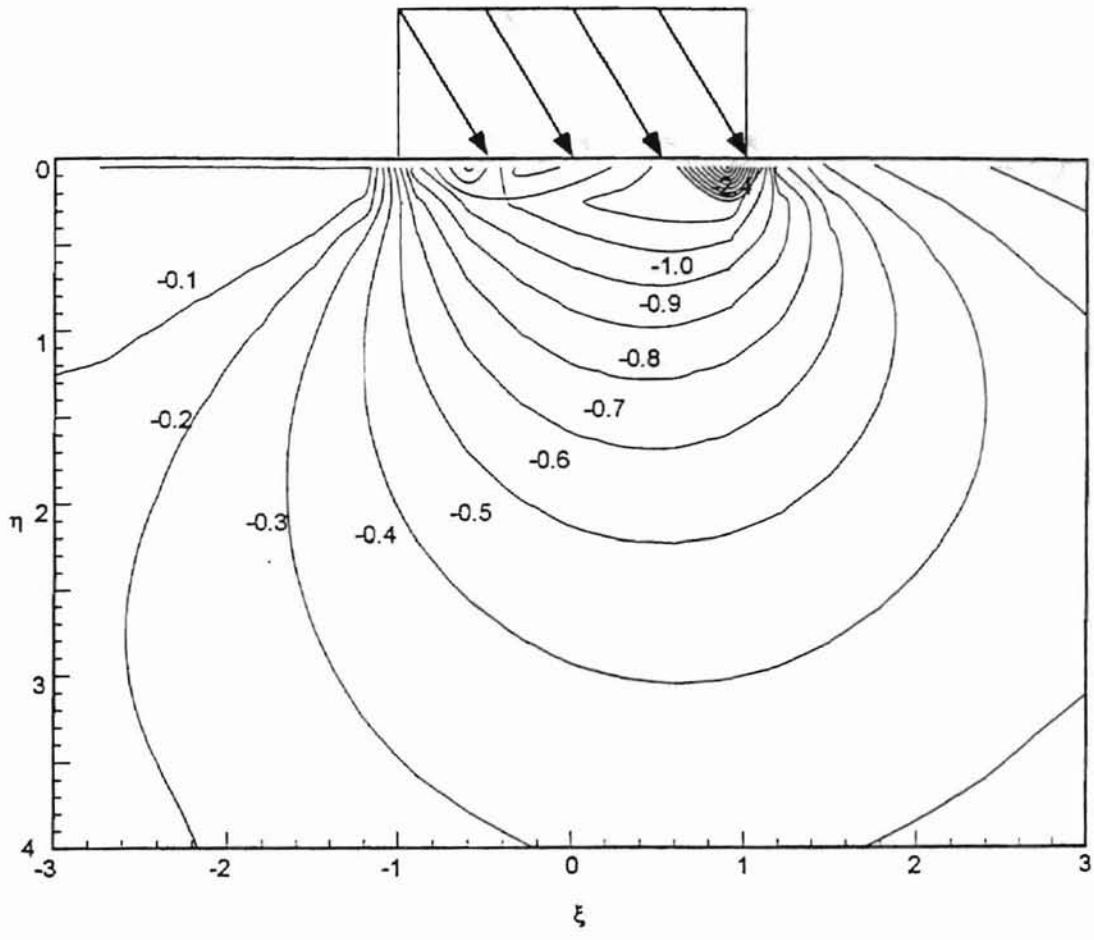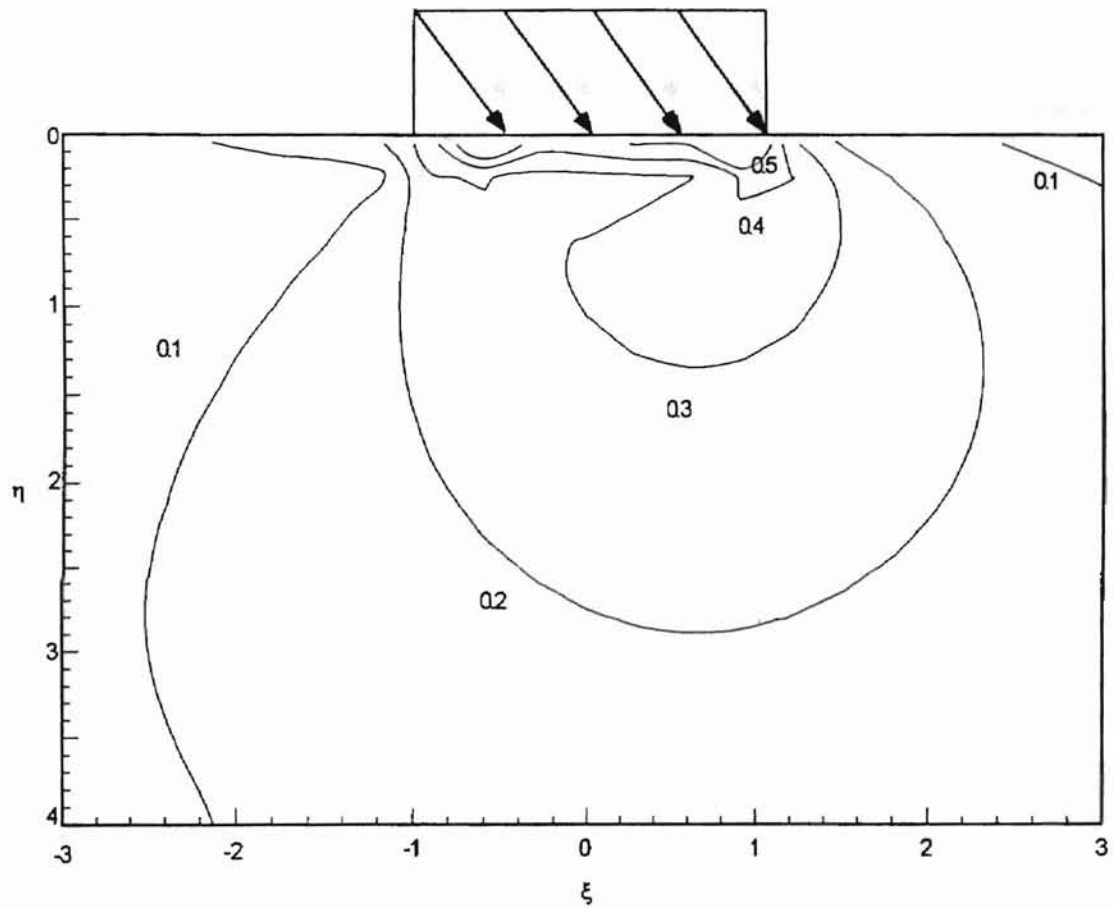
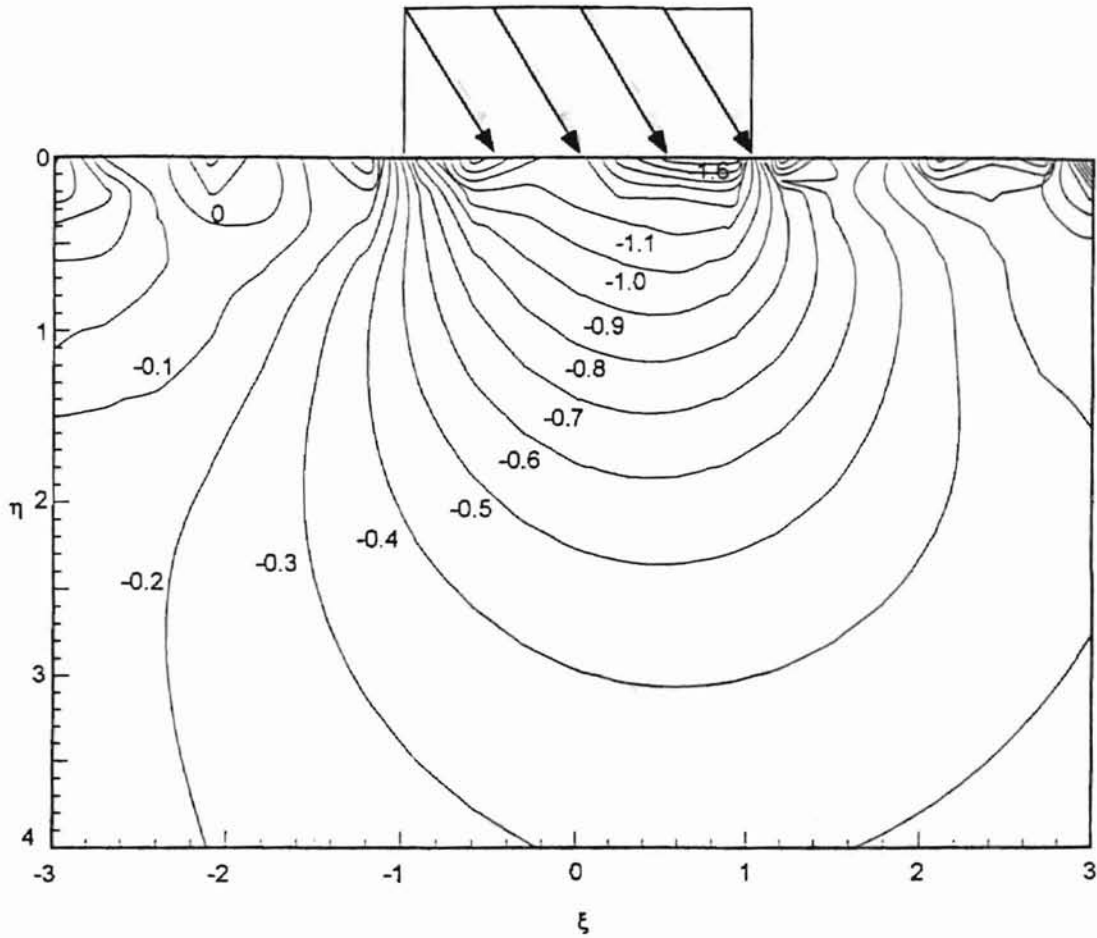Figure 3-14: Maximum Shear Stress for the Elastostatic Case with Constant Loading, $q_0 = 1/3p_0$.

31

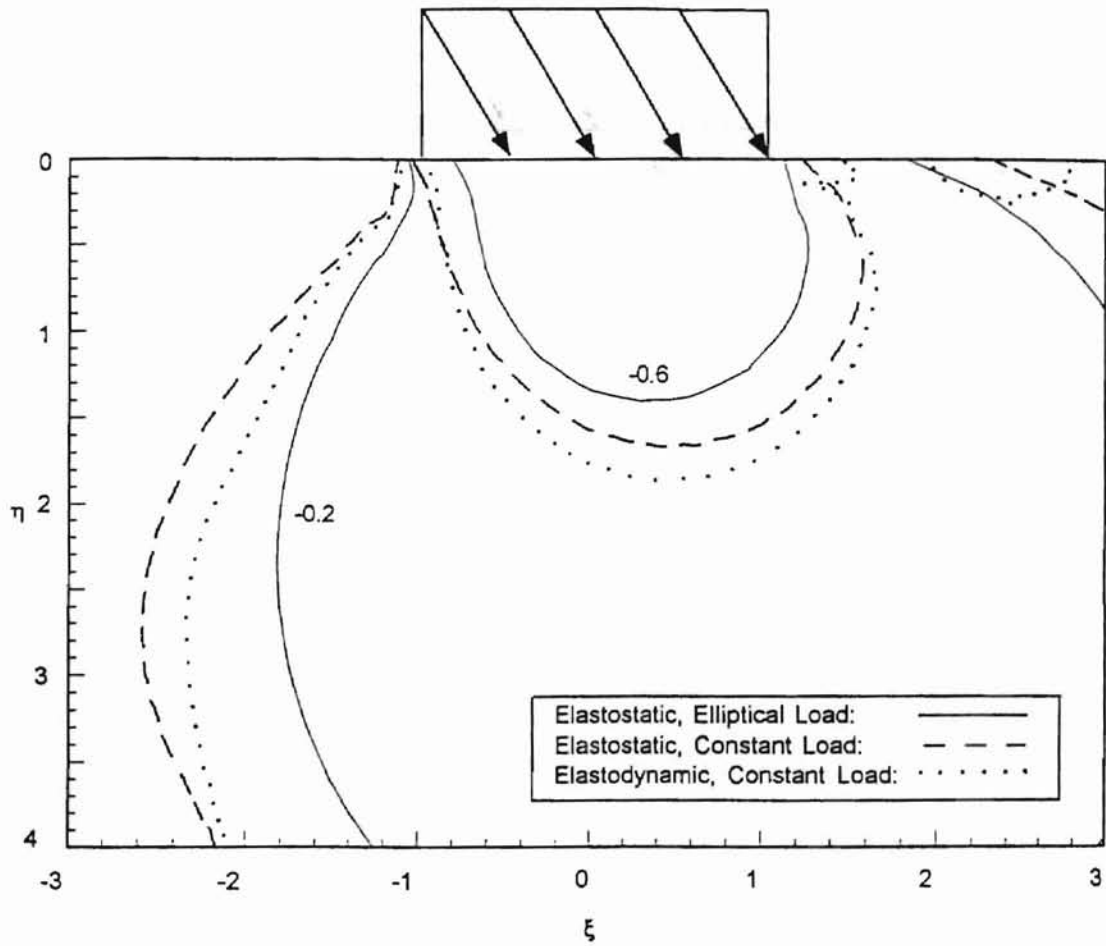Figure 3-15: Maximum Shear Stress for the Elastodynamic Case with Constant Loading, $q_0 = 1/3p_0$.
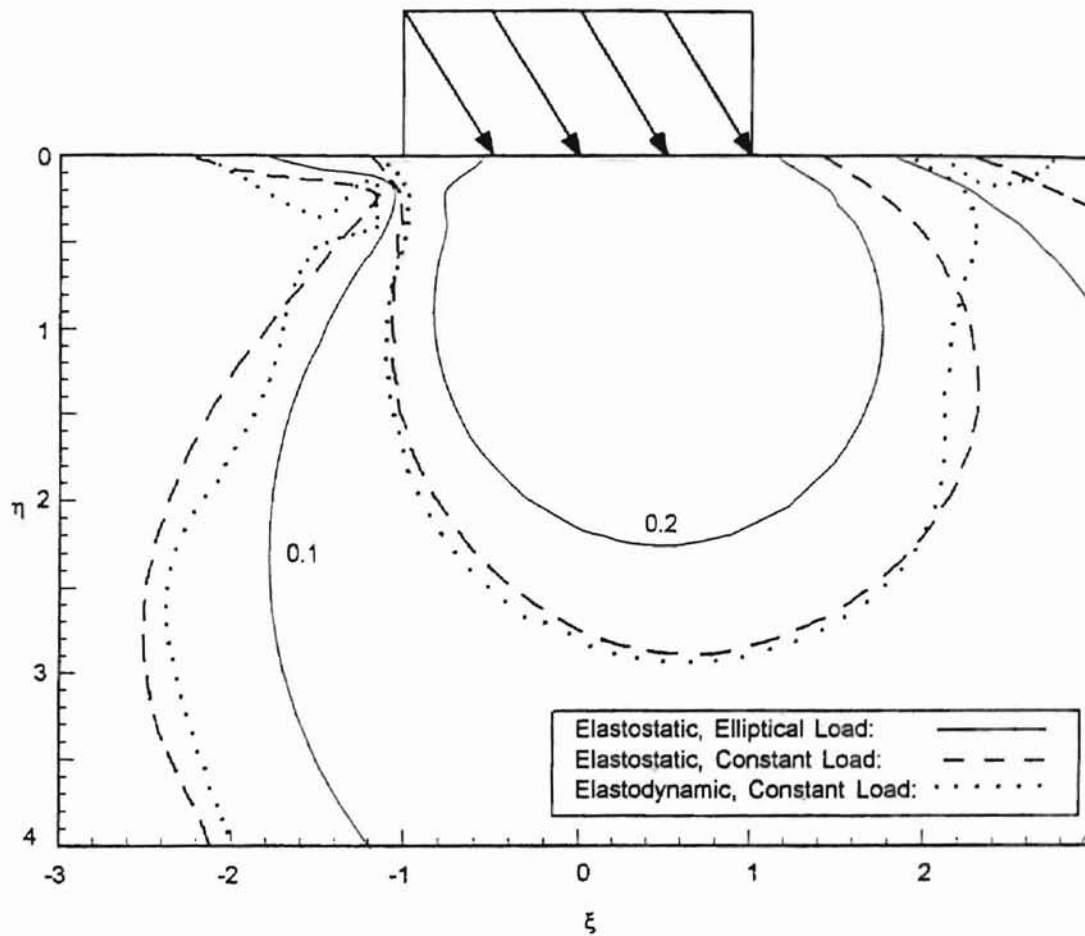
Figure 3-16: Comparison of the Maximum Shear Stress for the Elastostatic, Elliptical and Constant Load Cases, and the Elastodynamic, Constant Load Case, $q_0 = 1/3p_0$.
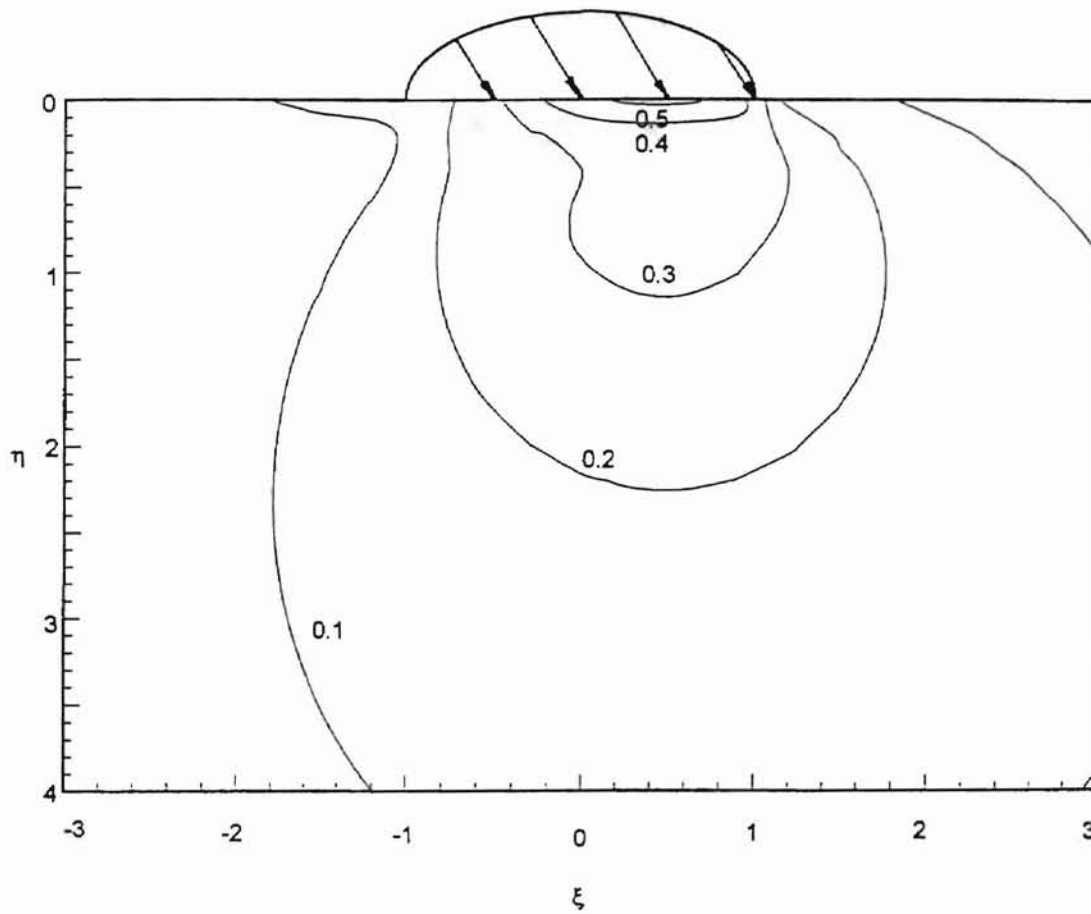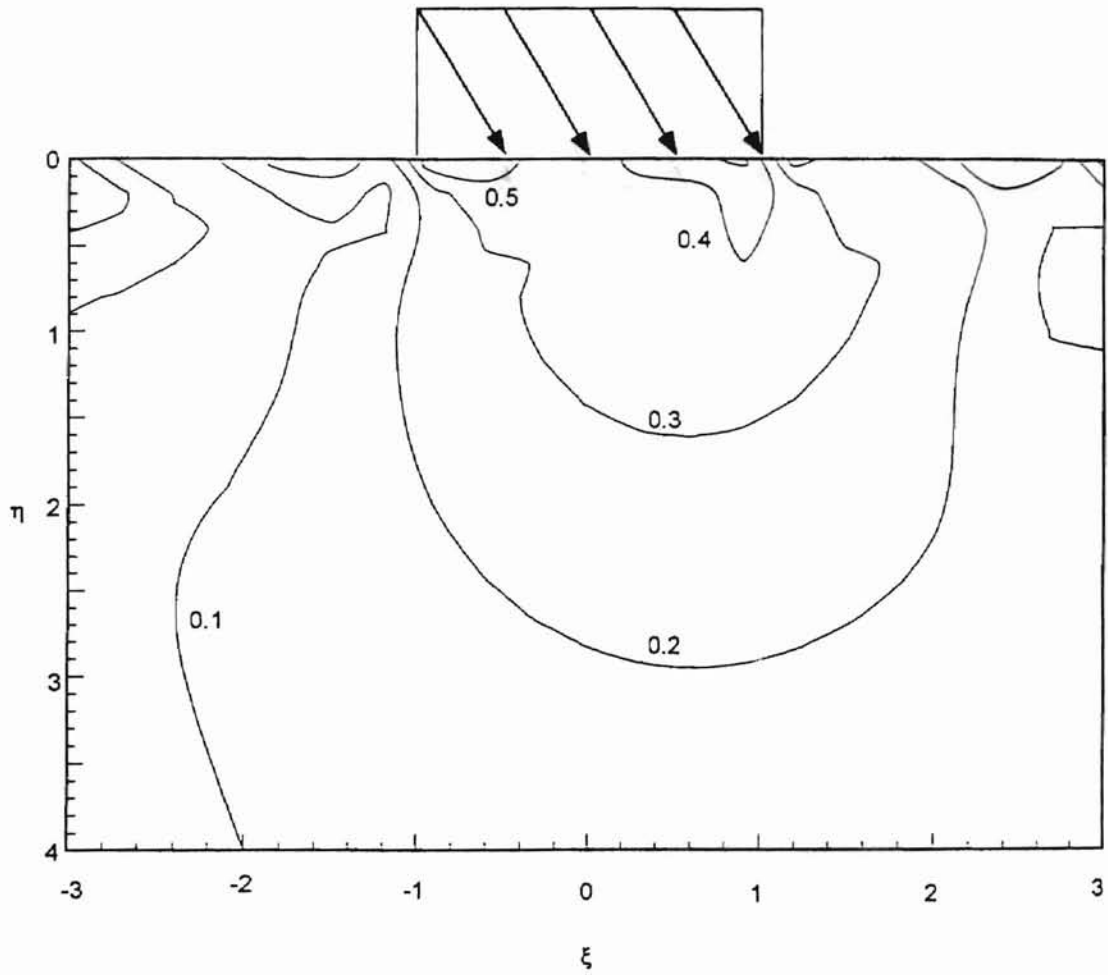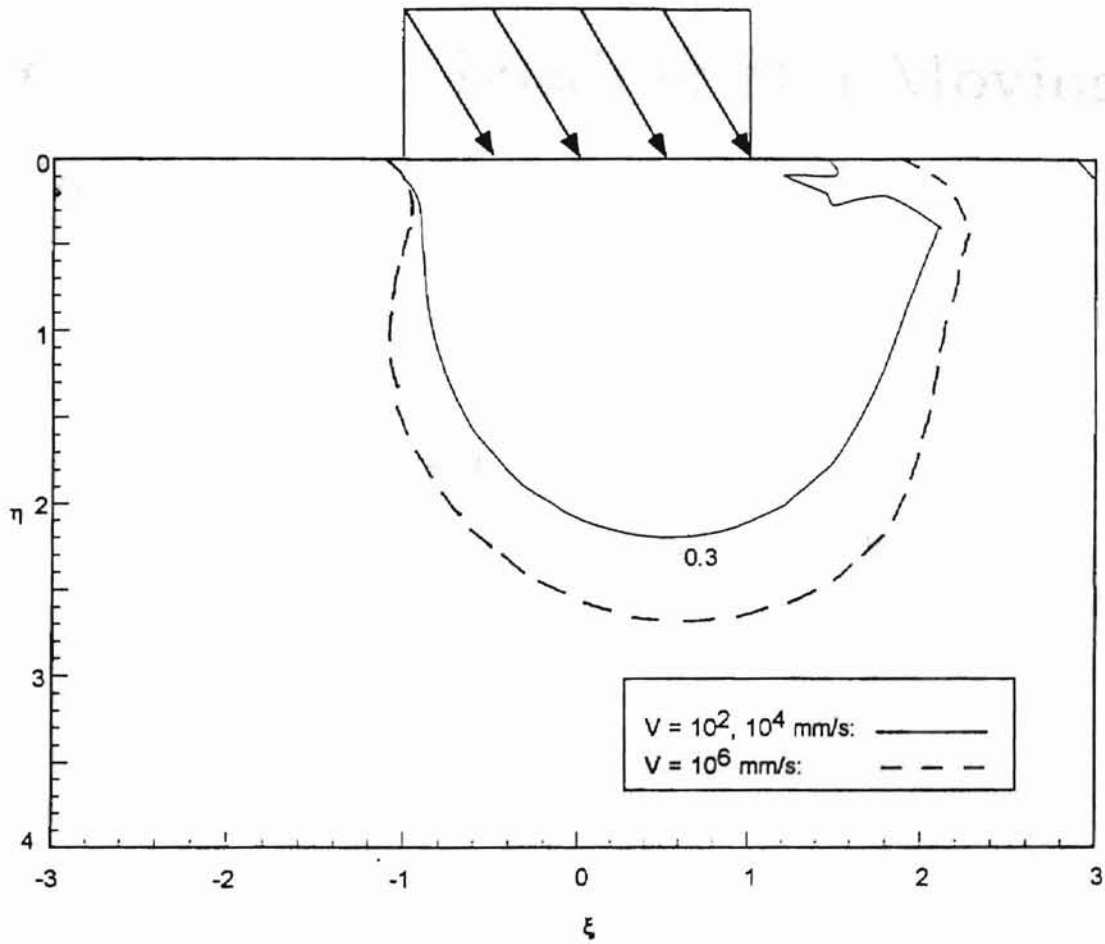
Figure 3-17: A Contour of the von Mises Equivalent Stress, Normalized by the Yield Strength, for Various Speeds.

Chapter 4

Elastoplastic Loading of a Moving Semi-Infinite Body

4.1 Elastoplastic Stress Field

4.1.1 Method of Merwin and Johnson

The elastoplastic stress field is determined by solving the Prandtl-Reuss equation using a Runge-Kutta method. The solution method is that of [12], as modified by [6]. A description of this approach, as presented in [16], is summarized below.

When the subsurface stress state reaches the yield condition, a plastic stress and strain relation may be applied. It is assumed the material behavior is elastic-perfectly plastic, that plane strain conditions exist, and the elastic deviatoric stress and strain are the initial conditions for the plastic stress and strain fields.

The total incremental strain is the sum of the incremental elastic strain and plastic strain:

$$\dot{e}_{ij} = \dot{e}_{ij}^{e} + \dot{e}_{ij}^{p} \tag{4.1}$$

The incremental plastic strain is obtained from the Levy-Mises equation:

$$\dot{e}_{ij}^{p} = \frac{\dot{w}^{p}}{2k^2} s_{ij} \tag{4.2}$$

where $\dot{w}^p$ is the incremental plastic work per unit volume, s_{ij} are the deviatoric stress components, and k is the yield strength in shear.

Using Hooke's law for the elastic strains, and the Levy-Mises equation for the plastic strains, the Prandtl-Reuss equation in terms of the incremental deviatoric stress and strain is:

$$\dot{e}_{ij} = \frac{\dot{s}_{ij}}{2G} + \frac{\dot{w}^p}{2k^2} s_{ij} \tag{4.3}$$

where G is the shear modulus. The energy rate per unit volume can be represented by the plastic energy, i.e., $\dot{w} = \dot{w}^p$. The deviatoric incremental stress is then:

$$\dot{s}_{ij} = 2G(\dot{e}_{ij} - \frac{\dot{w}^p}{2k^2} s_{ij}) \tag{4.4}$$

It is convenient to transform the time rates of change to gradients with respect to ξ as follows:

$$\frac{d}{dt}(\dot{s}_{ij}, \dot{e}_{ij}, \dot{w}^p) = V\frac{\partial}{\partial\xi}(\dot{s}_{ij}, \dot{e}_{ij}, \dot{w}^p) \tag{4.5}$$

At steady state, the time derivatives in Equations 4.5 vanish, so the speed V is eliminated from the equation.

4.1.2 Residual Stresses and Strains

The incremental deviatoric stress can be found with the Runge-Kutta method using the elastic stress fields starting from the first yield point at a given depth in the body. This stress field is used to calculate the stress field for the next point. At the end of a step at a given depth, the calculated stress may not satisfy the equilibrium condition, which is then satisfied by introducing residual stresses. For the calculation of residual stresses, Suh's procedure was used [6], [16]:

1. Initialize residual stresses and strains to zero.

2. Calculate elastic stresses along ξ-axis at fixed η.

3. When the stress state reaches the von Mises yield criterion, the Prandtl-Reuss equations are used to calculate the stresses for the subsequent point, assuming the total strains are the same as that given by the elastic solution.

36

4. The Prandtl-Reuss equations are integrated using a fourth-order Runga-Kutta scheme. Starting from the first yield point, the stress rates are found from Equations 4.5, using the already calculated stress gradients. These stress rates are used to predict the stress components of the next point.

5. If the yield criterion is not satisfied or the rate of plastic work becomes negative, plastic deformation ends. The stress at the next point is calculated from the elastic equation.

6. The final calculated state of stress violates the equilibrium condition. At the end of each iteration, the stresses are relaxed elastically to satisfy equilibrium, and residual stresses are calculated.

7. Steps 2-6 are repeated for the same point using the residual stresses from the previous iteration until a steady state is reached, where the residual stresses and strains are not significantly different from those of the previous iteration.

8. Step 7 is continued in the η-direction.

The possible residual stress components are independent of ξ due to the nature of the sliding problem and can be written as functions of η alone:

$$(\sigma_{\xi\xi})_r = f_1(\eta), \quad (\sigma_{\eta\eta})_r = f_2(\eta), \quad (\sigma_{\xi\eta})_r = f_3(\eta) \tag{4.6}$$

The equilibrium equations for residual stress are:

$$\frac{\partial(\sigma_{\xi\xi})_r}{\partial\xi} + \frac{\partial(\sigma_{\xi\eta})_r}{\partial\eta} = 0 \tag{4.7}$$

$$\frac{\partial(\sigma_{\xi\eta})_r}{\partial\xi} + \frac{\partial(\sigma_{\eta\eta})_r}{\partial\eta} = 0$$

Substituting Equations 4.6 into Equations 4.7,

$$f_2(\eta) = C_2, \quad f_3(\eta) = C_3 \tag{4.8}$$

where C_2 and C_3 are constants.

The boundary conditions for the residual stresses are:

$$(\sigma_{\eta\eta})_r = (\sigma_{\xi\eta})_r = 0 \ at \ (\xi, \eta) = (\infty, 0) \tag{4.9}$$

37

From these boundary conditions, C_2 and C_3 are zero, and the possible residual stresses for plane strain are:

$$(\sigma_{\xi\xi})_r = f(\eta), \ (\sigma_{\zeta\zeta})_r = \nu f(\eta), \ (\sigma_{\eta\eta})_r = (\sigma_{\xi\eta})_r = 0 \tag{4.10}$$

where ζ is the dimensionless width (i.e., $\zeta = z/l$). Since the equilibrium and residual stress boundary conditions are not satisfied at the end of each iteration, the state of stress at the end of each iteration gives non-zero "pseudo-residual stresses" for $(\sigma_{\eta\eta})'_r$ and $(\sigma_{\xi\eta})'_r$. These pseudo-residual stress components are the difference between the elastoplastic stress and the elastic stress at the point where the elastic-plastic boundary ends at the trailing edge at each iteration. The corresponding strains are:

$$(\varepsilon_{\eta\eta})_r = -\frac{1-2\nu}{2(1-\nu)G}(\sigma_{\eta\eta})'_r, \ (\gamma_{\xi\eta})_r = -\frac{(\sigma_{\xi\eta})'_r}{G} \tag{4.11}$$

Using the stress from each iteration, the residual stresses are:

$$(\sigma_{\xi\xi})_r = (\sigma_{\xi\xi})'_r - \frac{\nu}{1-\nu}(\sigma_{\eta\eta})'_r, \ (\sigma_{\zeta\zeta})_r = (\sigma_{\zeta\zeta})'_r - \frac{\nu}{1-\nu}(\sigma_{\eta\eta})'_r \tag{4.12}$$

These residual stresses are used as initial conditions for the iteration, until there is no change in $(\sigma_{\xi\xi})_r$ and $(\sigma_{\zeta\zeta})_r$. As was the case with the elastic stress fields, the singularities at the ends of the slider cause error in the residual stresses at depths near the surface.

4.2 Residual Stresses by the Finite Element Method

Suh [16] reports the use of the finite element method by H.-C. Sin (Ph.D. thesis, Massachusetts Institute of Technology, 1981) to model the plastic deformation of a semi-infinite elastic-perfectly plastic solid under cyclic loading by asperities (sliders). The residual stress $(\sigma_{\xi\xi})_r$, shown in Figure 4-1 (from [16]) after one, two, three and four passes of an asperity, exerting an elliptical load on the surface, is tensile near the surface, then compressive and larger at a greater depth, with smaller tensile stress at a still greater depth. After four passes, there is negligible difference in the residual stress. The results obtained from

38

this method have generally been in good agreement with those obtained from the Merwin-Johnson method. Repeated cyclic loading would be similar to the conditions found in ultra-precision machining.
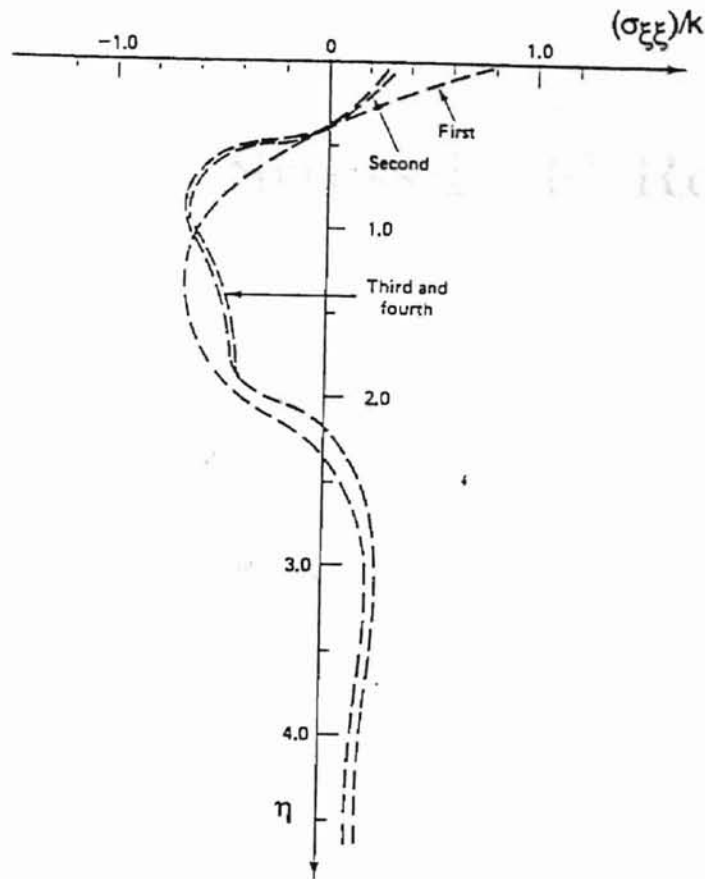

Figure 4-1: Variation of Sliding Directional Residual Stress as a Function of Depth Under a Moving Asperity.

Chapter 5

Elastoplastic Stress Field Results

This chapter presents a verification of the residual stresses from the Merwin-Johnson method as implemented in the corrected program upon changing the stress gradients from Equations 2.16 to Equations 2.17. Data obtained from the orthogonal flycutting of Al 6061-T6 and Te-Cu [13] are then used to predict the elastoplastic stress contours and residual stresses in the cutting direction using the corrected program.

5.1   Verification of Residual Stresses

Figure 5-1 shows the residual stresses in the cutting direction as predicted by the corrected program for an elastodynamic, constant surface load using the Merwin-Johnson method with a step size of 0.05 in the ξ- and η-directions for comparison with those of Figure 4-1. Shown are the results after five iterations, after which there is a negligible difference. The material properties used are [16]: isotropic, slightly work hardening (slope of the work-hardening region $= 10^{-4}$ E, where E is Young's modulus), E=1.96×10^5 MPa $= 2 \times 10^4$ kg/mm^2, $\nu = 0.28$, and the yield strength in shear, k, is 25.0 kg/mm^2. The normal and tangential loads are 4k and k, respectively. The stresses are normalized with respect to k. Since the material density is used to calculate elastodynamic stresses and was not specified in [16], the density of Te-Cu, 9.14×10^{-10} was used. A speed of 125 mm/s was used.

Compared to the curve marked "third and fourth" in Figure 4-1, it can be seen that the trend is the same: tensile stresses near the surface, becoming compressive at approximately
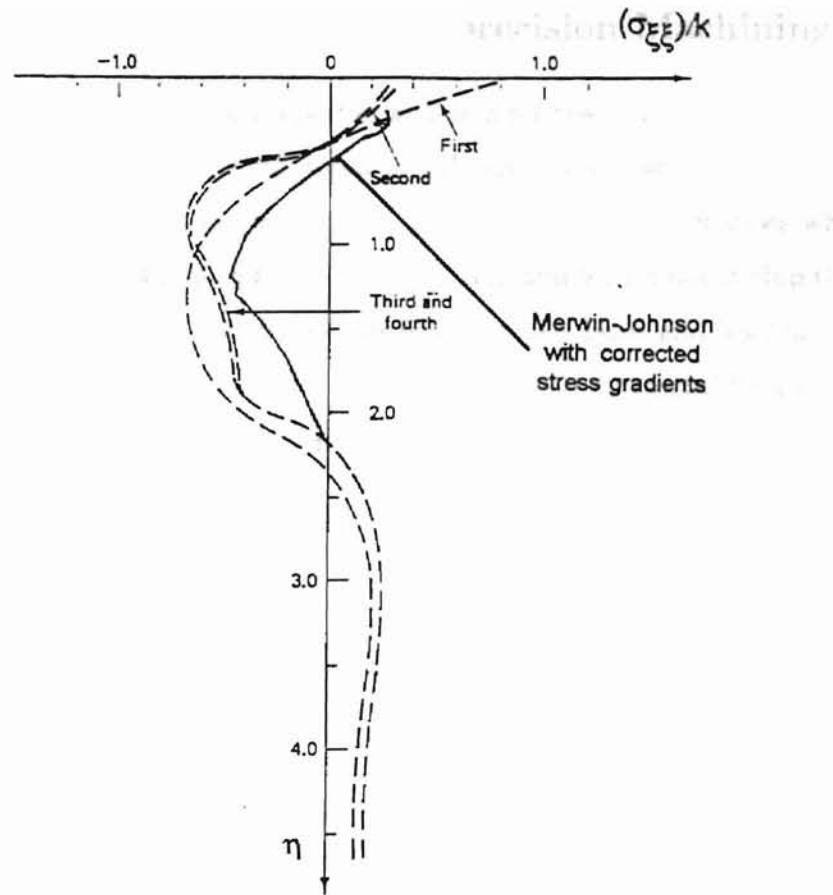
Figure 5-1: Comparison of the Results from the Corrected Program Using the Merwin-Johnson Method with the FEM Solution.

$\eta = 0.5$ and zero at $\eta = 2.25$. The maximum compressive stress occurs at $\eta = 1.2$, and this maximum stress is within roughly 33% of that predicted by the finite element model. This difference is smaller at greater depths. Overall the results of the Merwin-Johnson method using an elastodynamic, constant surface load are in general agreement with those of the FEM solution using an elliptical surface load.

5.2 Elastoplastic Stress Field Results for Surface Loading Conditions Measured in Ultra-precision Machining

Tables 5.1 and 5.2 show the material properties and data for the ultra-precision machining experiments of [13], in which a cutting speed of 125 mm/s was used. Since the sliding indentation model is considered applicable only in those sub-micrometer cases where the cutting force is less than the thrust force, only the 0.01μm and 0.1μm uncut chip thickness cases will be considered. In the modeling of elastoplastic stress fields and residual stresses, the thrust (F_t) and cutting (F_c) forces replace the vertical and horizontal forces P and Q of Figure 2-1. That is, $\mu_f = \frac{F_c}{F_t}$ in Equations 2.15 and 2.17.

Al 6061-T6 Workpiece	Properties
Young's Modulus (E)	72.4 (GPa)
Poisson's ratio (ν)	0.33
Mass density (ρ)	2.821×10^{-10} (kg/mm^2)
Yield Strength (Y)	363 (MPa)

Te-Cu Workpiece	Properties
Young's Modulus (E)	120 (GPa)
Poisson's Ratio (ν)	0.3
Mass density (ρ)	9.14×10^{-10} (kg/mm^2)
Yield Strength (Y)	225 (MPa)

Table 5.1. Workpiece Material Properties

Uncut Chip Thickness (μm)	F_c (N/mm)	F_t (N/mm)	l (μm)
Al 6061-T6			
0.01	0.173	0.531	0.515
0.1	0.563	0.586	0.537
Te-Cu			
0.01	0.214	0.547	1.0
0.1	0.319	0.491	1.0

Table 5.2. Measured Force Components and Contact Lengths for Orthogonal Flycutting

43

Figures 5-2 through 5-5 show the von Mises elastoplastic stress fields for Al 6061-T6 and Te-Cu for the two uncut chip thicknesses, normalized with respect to the uniaxial yield strength. The plots were prepared using a step size of 0.05 in both the ξ- and η-directions and cover the range $\xi = [-3,3]$ and $\eta = [0,4]$.

A plot of the von Mises elastoplastic stress field using a step size of 0.01 in the ξ- and η-directions for Al 6061-T6 for the 0.01μm uncut chip thickness case in shown in Figure 5-6. This plot shows little difference from that using the 0.05 step size, so the other plots for a step size of 0.01 are not included here.

The plots show the elastic-plastic boundary ($\sigma_{eq}/Y = 1$). In each of the four cases the boundary is shifted toward the leading edge. Te-Cu being of lower yield strength, exhibits a plastic deformation zone which is much larger for a given uncut chip thickness. The actual depth of the predicted plastic zone is somewhat different than that shown by these contours as a result of the way the plotting software smooths the data. For uncut chip thicknesses of 0.01 and 0.1μm the depth of the plastic zone is 0.65η and 1.6η for Al 6061-T6 and 0.4η and 0.55η for Te-Cu. For diamond turning of an aluminum alloy, it has been found [15] that the "work-affected" layer is on the order of sub-micrometers using X-ray diffraction analysis. This is consistent with the results found here.

5.3   Estimated Residual Stresses

Using the Merwin-Johnson method, residual stresses for the cutting direction were predicted in the plastic layers of the Al 6061-T6 and Te-Cu workpieces at 0.01μm and 0.1μm uncut chip thicknesses, as shown in Figures 5-7 through 5-10. These stresses are normalized with respect to the yield strength. For these cases ten iterations were used; only five were required in the verification of the method above, in which case the forces involved were roughly four times as large. While it was unnecessary to use a step size smaller than 0.05 for the elastoplastic stress fields, the use of that step size yielded plots of very few points for shallow plastic zone cases. Therefore, the residual stress plots were prepared using a step size of 0.01. Figures 5-11 and 5-12 show the residual stress results from [13], with

44

the uncorrected stress gradients. It can be seen that the trend is much unlike that shown in Figure 5-1. At 0.01μm and 0.1μm uncut chip thicknesses, the maximum compressive residual stresses for Al 6061-T6 are 29 MPa and 102 MPa, and 16 MPA and 27 MPA for Te-Cu.

As they were above, the cutting-directional residual stresses are tensile near the surface and then become compressive. Only the shallow tensile and deeper compressive plastic residual stresses are calculated by the program. To agree with the trend of the FEM solution, the residual stresses at greater depths should be tensile and elastic. The general trend in the residual stresses for the Al 6061 T6 more closely matches that of the verification above because the plastic zones are deeper. It should be noted that the residual stresses near the surface may actually be elastic for the proper combination of applied loads and material properties [6], [16], resulting in a subsurface plastic zone. Therefore it is not only unclear that the magnitudes of the residual stresses predicted near the surface are correct, but also whether they are actually plastic at these depths.
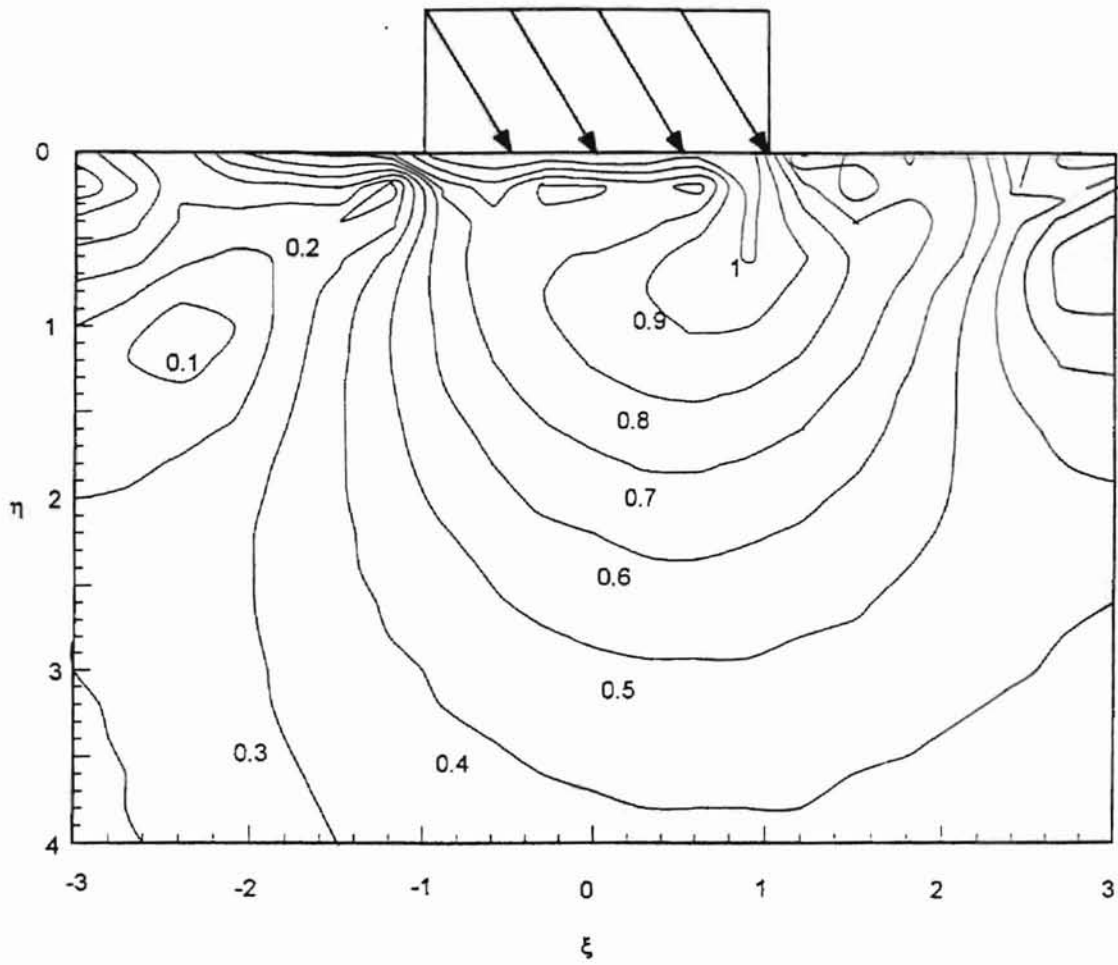
Figure 5-2: Contours of the von Mises Equivalent Stress, Normalized by the Yield Strength, for Al 6061-T6 for 0.01μm Uncut Chip Thickness.
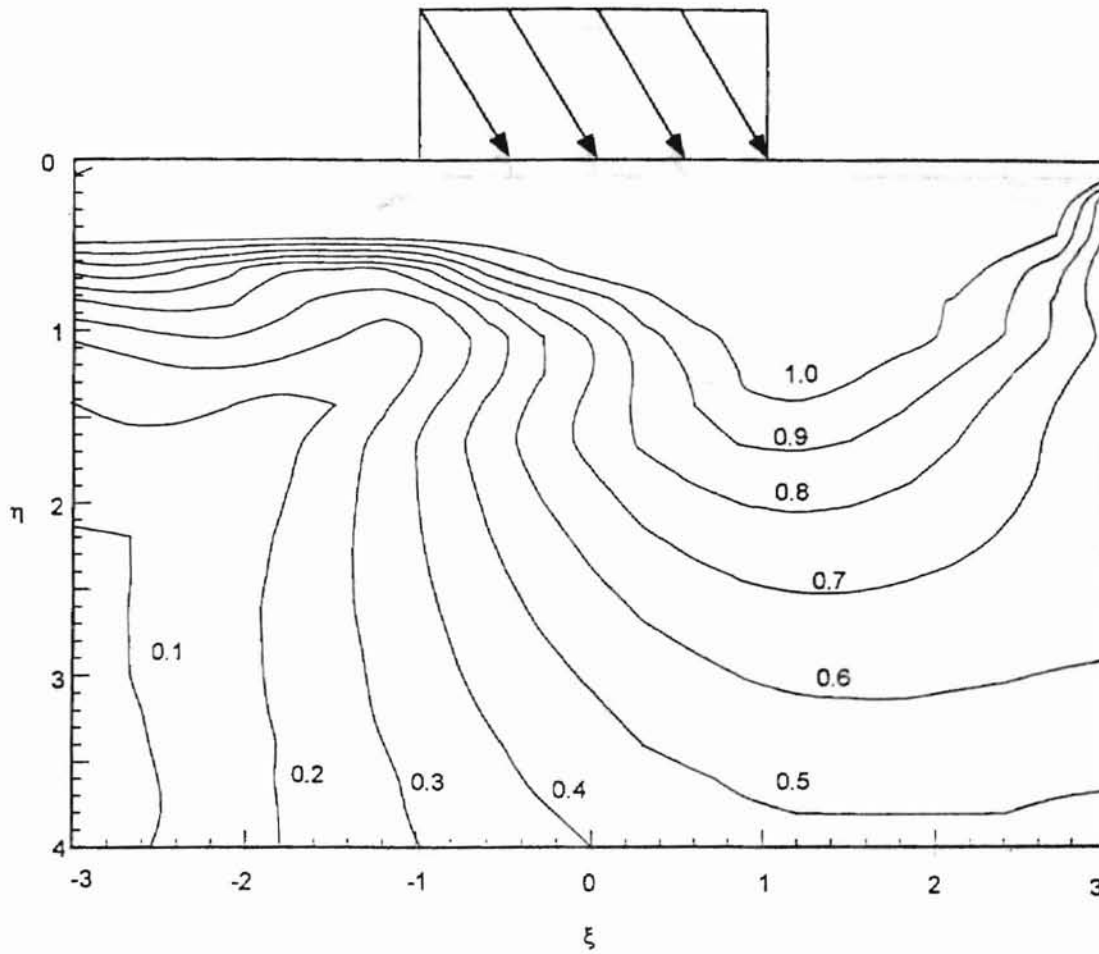
Figure 5-3: Contours of the von Mises Equivalent Stress, Normalized by the Yield Strength, for Al 6061-T6 for 0.1μm Uncut Chip Thickness.
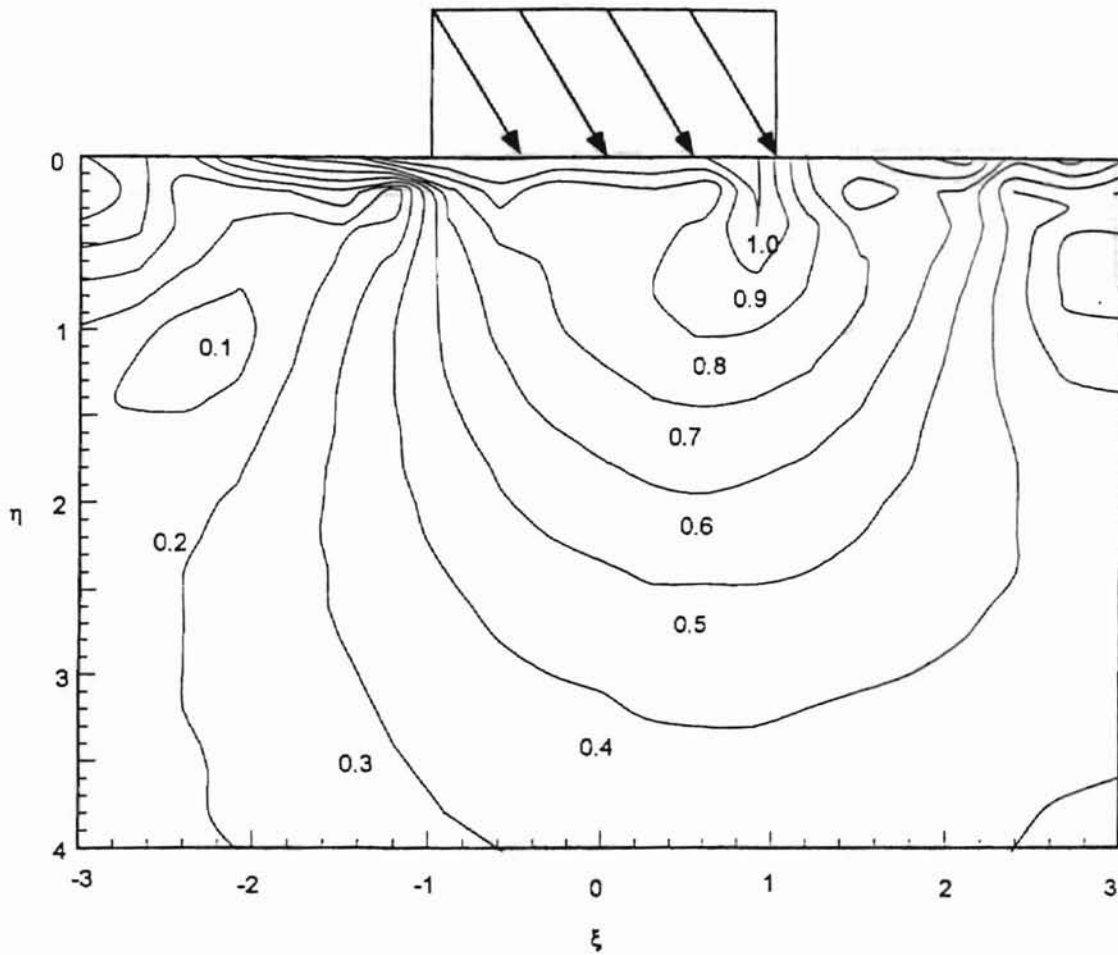
Figure 5-4: Contours of the von Mises Equivalent Stress, Normalized by the Yield Strength, for Te-Cu for 0.01μm Uncut Chip Thickness.
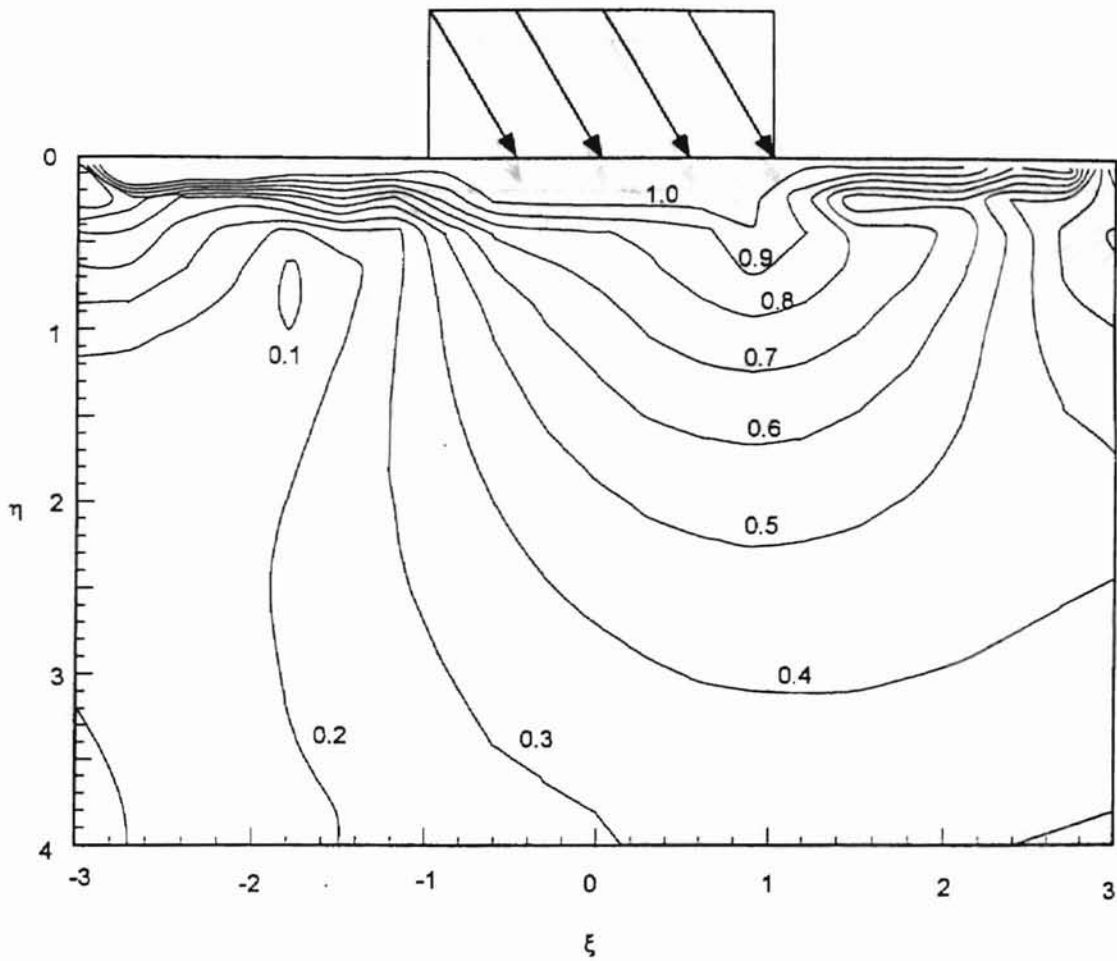
Figure 5-5: Contours of the von Mises Equivalent Stress, Normalized by the Yield Strength, for Te-Cu for 0.1μm Uncut Chip Thickness.
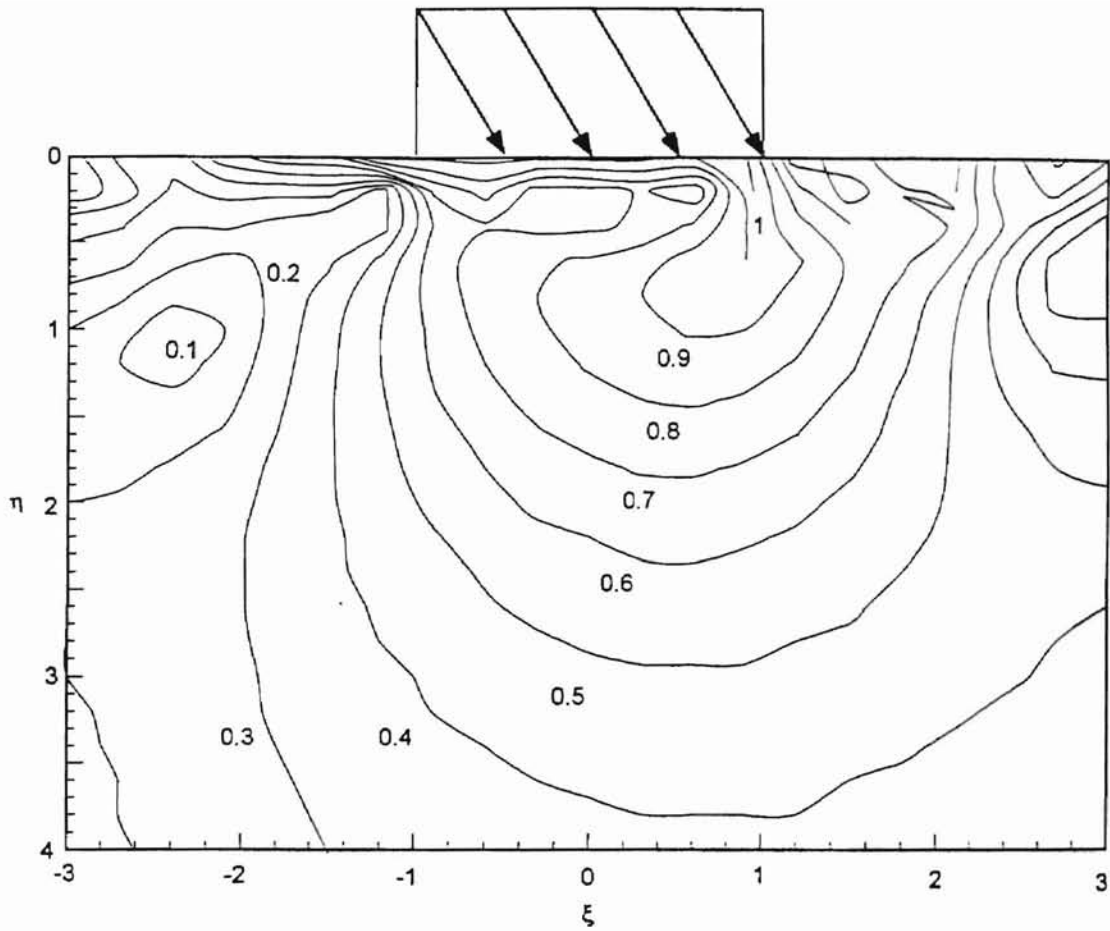
Figure 5-6: Contours of the von Mises Equivalent Stress for a Reduced Step Size of 0.01, Normalized by the Yield Strength, for Al 6061-T6 for $0.01\mu m$ Uncut Chip Thickness.
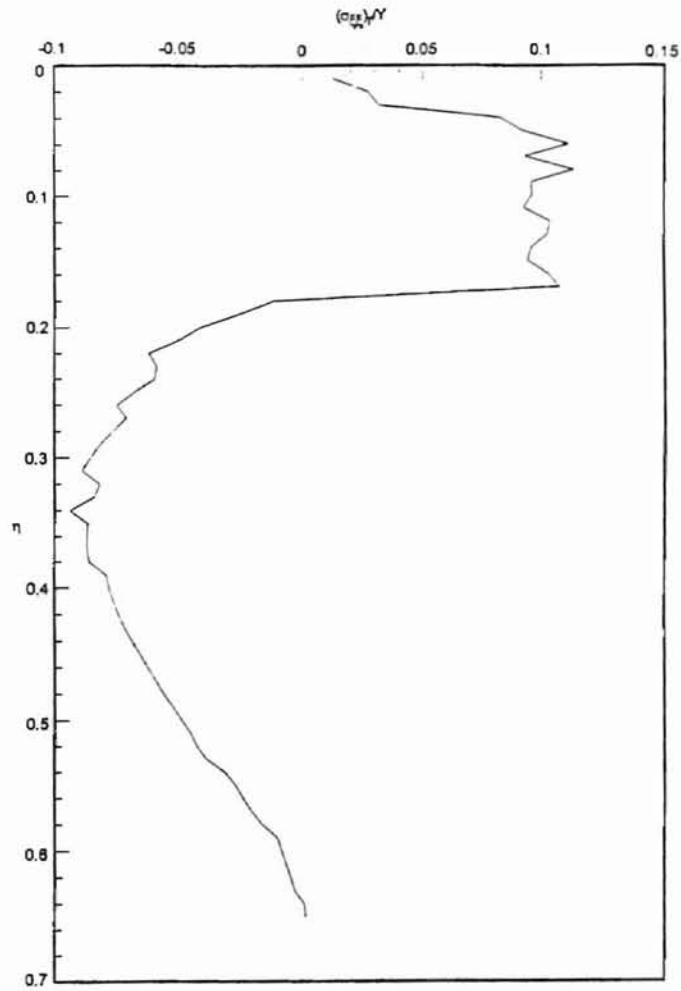
Figure 5-7: Normalized Cutting Directional Residual Stress for Al 6061-T6 Predicted for 0.01μm Uncut Chip Thickness.

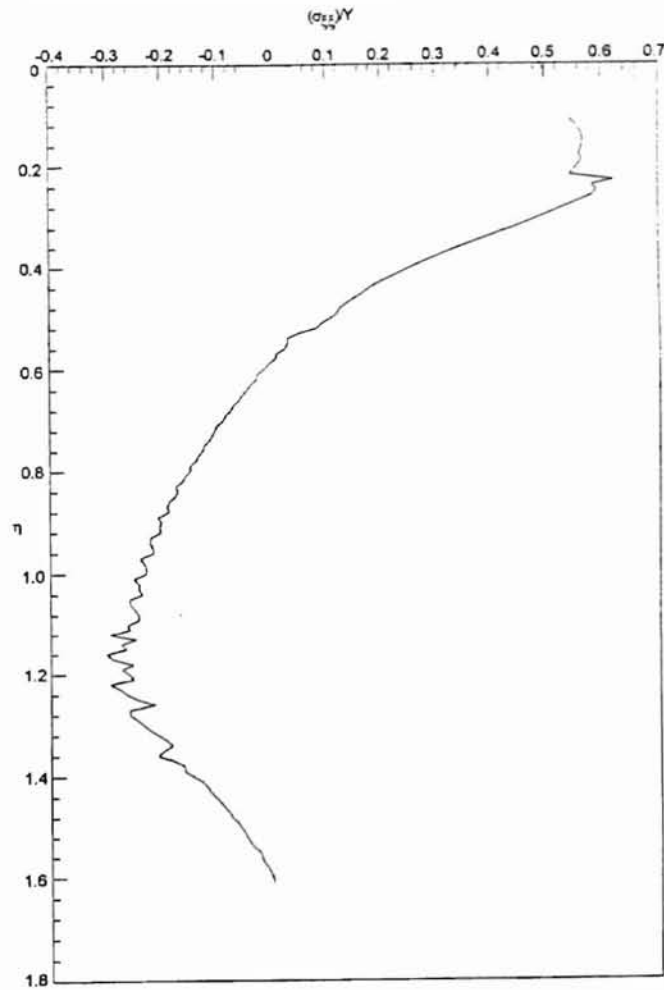Figure 5-8: Normalized Cutting Directional Residual Stress Predicted for Al 6061-T6 for 0.1μm Uncut Chip Thickness.
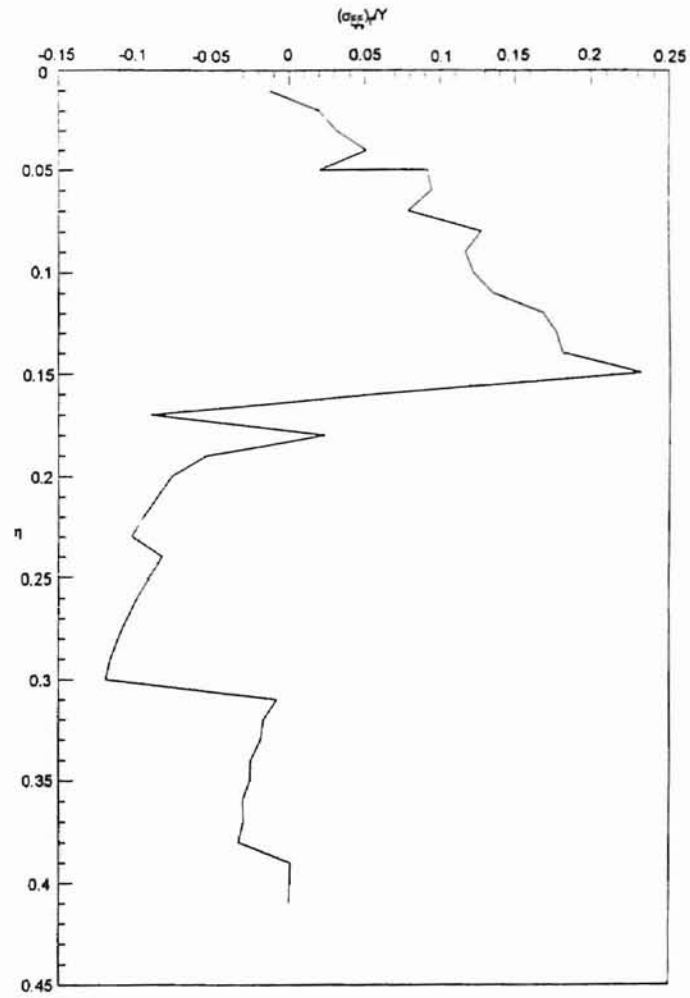
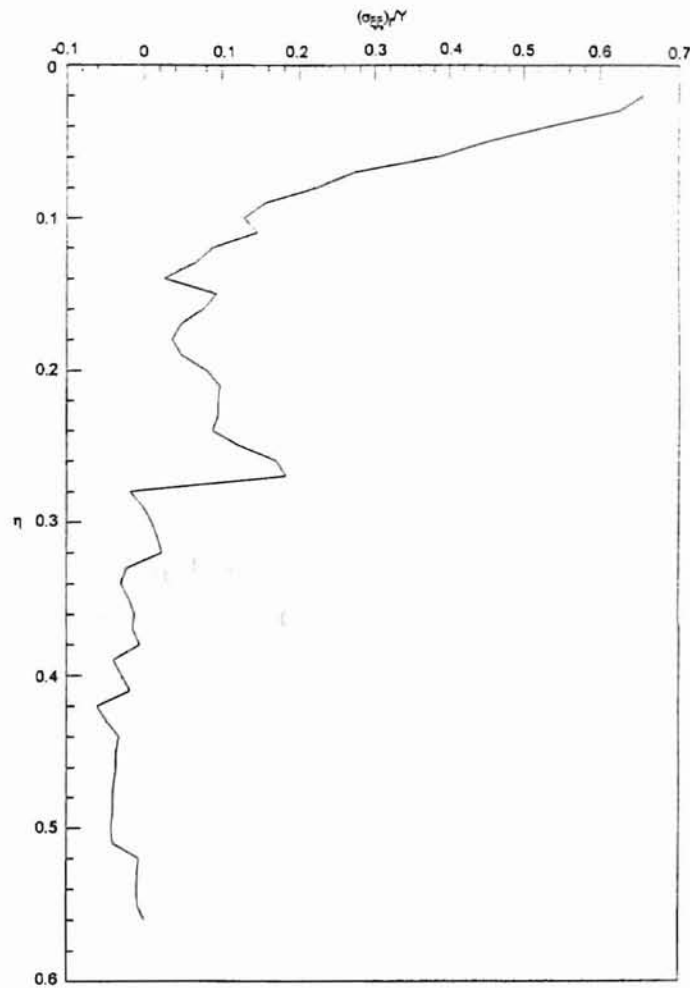Figure 5-9: Normalized Cutting Directional Residual Stresses for Te-Cu for 0.01 Uncut Chip Thickness.

53

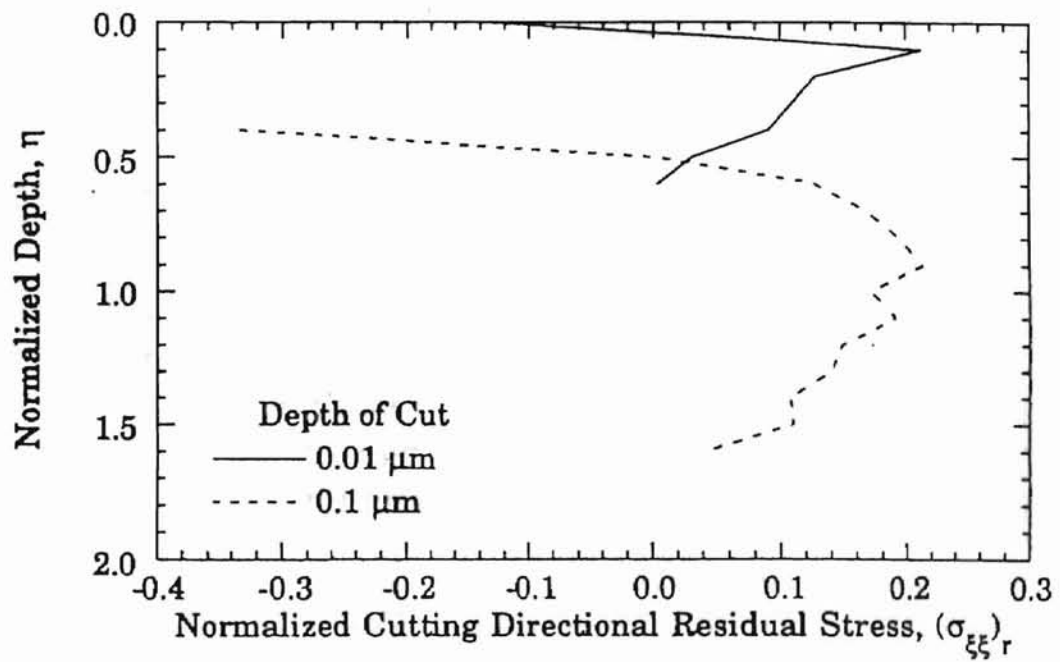Figure 5-10: Normalized Cutting Directional Residual Stress for Te-Cu for 0.1μm Uncut Chip Thickness.

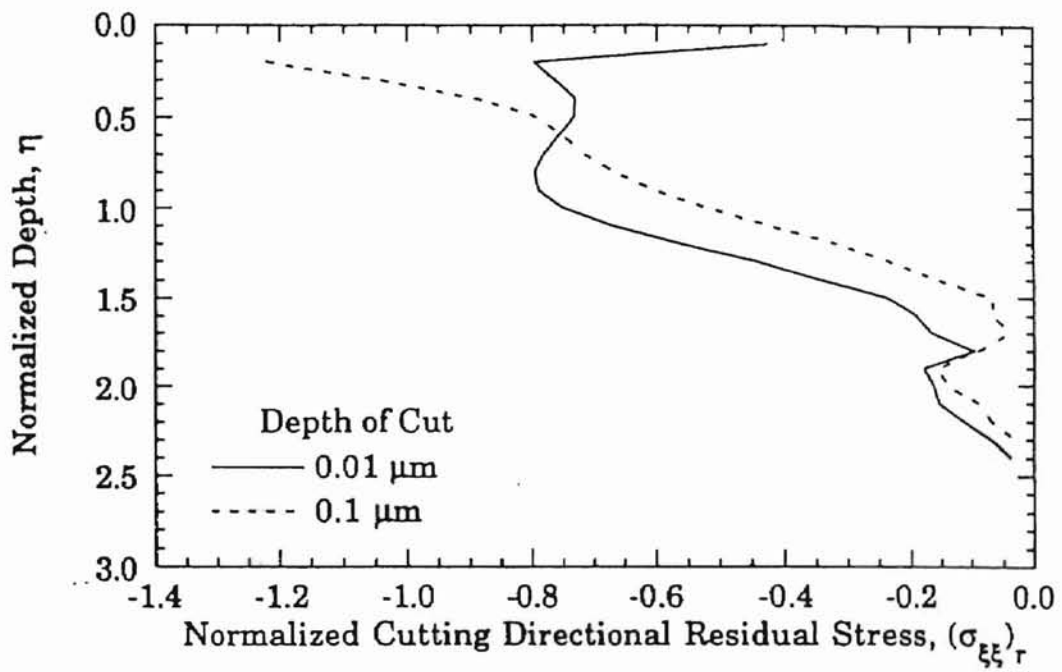Figure 5-11: Normalized Cutting Directional Residual Stresses for Al 6061-T6 Using Uncorrected Stress Gradients.

Figure 5-12: Normalized Cutting Directional Residual Stresses for Te-Cu Using Uncorrected Stress Gradients.

Chapter 6

Conclusion

The calculation of elastoplastic stress fields and residual stresses in an elastic-plastic half-space by the Merwin-Johnson required accurate elastic stress fields and sliding-direction stress gradients. A constant surface pressure distribution being the most likely to model the tool-workpiece interaction in ultra-precision machining, it was used in the elastodynamic model and in the elastoplastic model for residual stresses. These stresses were verified as follows:

1. The stress fields for the constant surface pressure elastostatic case were compared against those for elliptical surface pressure for the case given in [14] and were found to be similar except near the slider, in accord with Saint Venant's principle.

2. For the small shear and dilatation wave speeds encountered in the experiments of [13], the dynamic effects should be small and a comparison with the static case is possible. At these speeds the elastostatic and elastodynamic constant surface pressure stress fields were nearly identical away from the surface, and so the elastodynamic stress fields were judged to be correct.

Having corrected the expressions for sliding-direction stress gradients, the Merwin-Johnson method was used to predict the depth of the plastic layer and the cutting (sliding) direction residual stresses for Al 6061-T6 and Te-Cu at 0.01 and 0.1 uncut chip thicknesses.

Bibliography

[1] R. Benjumea and D. L. Sikarskie. On the solution of plane, orthotropic elasticity problems by an integral method. *Journal of Applied Mechanics*, 39(3):801–808, 1972.

[2] H. L. Bjarnehed. Rigid punch on stressed orthotropic half-plane with partial slip. *Journal of Applied Mechanics*, 58(1):128–133, 1991.

[3] V. I. Fabrikant. Inclined flat punch of arbitrary shape on an elastic half-space. *Journal of Applied Mechanics*, 53(4):798–806, 1986.

[4] G. M. Hamilton and L. E. Goodman. The stress field created by a circular sliding contact. *Journal of Applied Mechanics*, 33(2):371–376, 1966.

[5] C. Hardy, C. N. Baronet, and G. V. Tordion. The elasto-plastic indentation of a half-space by a rigid sphere. *International Journal for Numerical methods in Engineering*, 3(4):451–462, 1971.

[6] S. Jahanmir. *A Fundamental Study on the Delamination Theory of Wear*. PhD thesis, Massachusetts Institute of Technology, 1977.

[7] K. L. Johnson. *Engineering Plasticity*. Cambridge University Press, 1968.

[8] J. W. Klintworth and W. J. Stronge. Plane punch indentation of anisotropic elastic half space. *Journal of Applied Mechanics*, 57(1):84–90, 1990.

[9] F. F. Ling. *Surface Mechanics*. John Wiley, 1973.

[10] D. A. Lucca and Y. W. Seo. Sliding indentation model of the tool-workpiece interface in ultra-precision machining. *Tribology Symposium of the Petroleum Division of the Amereican Society of Mechanical Engineers*, 61:17–22, 1994.

[11] D. A. Lucca, Y. W. Seo, and R. L. Rhorer. Energy dissipation and tool-workpiece contact in ultra-precision machining. *STLE Tribology Transactions*, 37(3):651–655, 1994.

[12] J. E. Merwin and K. L. Johnson. An analysis of plastic deformation in rolling contact. *Proceedings of the Institution of Mechanical Engineers*, 177(25):676–690, 1963.

[13] Y. W. Seo. *Energy Dissipation in Orthogonal Ultra-precision Machining of Ductile Materials*. PhD thesis, Oklahoma State University, 1993.

[14] J. O. Smith and C. K. Liu. Stresses due to tangential and normal loads on an elastic solid with application to some contact stress problems. *Journal of Applied Mechanics*, 20(2):157–166, 1953.

[15] T. Sugano, K. Takeuchi, and Y. Yoshida. Diamond turning of an aluminum alloy for mirror. *Annals of the CIRP*, 36(1):17–20, 1987.

[16] N. P. Suh. *Tribophysics*. Prentice-Hall, 1986.

VITA

Andrew Charles Loeber

Candidate for the Degree of

Master of Science

Thesis: PREDICTION OF THE SUBSURFACE STRESS STATE IN A MOVING SEMI-INFINITE
             SOLID FOR LOADING CONDITIONS REPRESENTING TOOL-WORKPIECE
             CONTACT IN ULTRA-PRECISION MACHINING

Major Field: Mechanical Engineering

Biographical:

   Education: Graduated from Richmond Senior High School, Richmond, Indiana in May, 1981;
       received Bachelor of Science degree in Industrial Engineering from Purdue University, West
       Lafayette, Indiana, in May, 1988; received Bachelor of Science degree in Mechanical
       Engineering from Montana State University, Bozeman, Montana, in May, 1992. Completed the
       requirements for the Master of Science with a major in Mechanical Engineering at Oklahoma
       State University in December, 1996.

   Experience: Employed by Perfect Circle, 1988-1989 as an industrial engineer; employed by Montana
       State University 1991-1992 and Oklahoma State University, 1994 as a teaching assistant.

   Professional Memberships: American Society of Mechanical Engineers, Alpha Pi Mu and Tau Beta Pi
       engineering honoraries.